FOSSIL ENERGY

DOE/ET/15611-7
(DE82010173)

A HIGH MAGNETIC FIELD MHD GENERATOR PROGRAM

Quarterly Report for the Period July 1—September 30, 1981

October 1981
Date Published

Work Performed Under Contract No. AC01-80ET15611

Stanford University
Stanford, California

U. S. DEPARTMENT OF ENERGY

DISCLAIMER

DOE/ET/15611-7
(DE82010173)
Distribution Categories UC-90g and UC-93

A HIGH MAGNETIC FIELD MHD GENERATOR PROGRAM

QUARTERLY REPORT

for the period

July 1, 1981 - September 30, 1981

Stanford University
Stanford, California 94305

Date Published - October 1981

Prepared for

THE UNITED STATES DEPARTMENT OF ENERGY

Under Contract DE-AC01-80ET15611

FOREWORD

Much of the work on this program is carried out by student Research Assistants and High Temperature Gasdynamics Laboratory staff members in addition to the Principal Investigators. The additional persons involved in a major way with the work reported here are

Mr. Brad Bennet
Mr. Wahid Hermina
Mr. Richard Heydt
Mr. John Reis
Mr. Dennis Roseman
Mr. Tad Simons
Mr. Craig Wynn

ABSTRACT

This report describes progress in an experimental and theoretical program designed to investigate a number of important problems in the development of MHD generator channels. The areas of research include nonuniformity and stability effects, boundary layers, Hall field breakdown, the effects of electrode configuration and current concentrations, and studies of steady-state combustion disk and linear channels in a 6 Tesla magnet of small dimensions.

In the area of magneto-acoustic disturbances, a major experiment to study the formation and behavior of propagating waves in a combustion MHD was completed, using the M-2 facility. The results of this experiment are currently being compared with a theoretical model previously developed at Stanford. For the study of the effects of nonuniformities on generator performance, a diagnostic system for measurement of plasma temperature profiles and also a nitrogen injection device were satisfactorily tested in the M-2 flowtrain.

An improved laser Doppler velocimeter system for the study of turbulence suppression in a magnetic field has been developed and tested, both on the bench and with the MHD flowtrain. A complex statistical analysis code for the interpretation of data of forthcoming turbulence suppression and MHD boundary layer experiments has been written and tested.

The theoretical model of Hall field breakdown has been modified to better account for the effects of current concentrations. The model now includes the capability to couple an "exact" solution for the plasma current distribution with the boundary layer and two-dimensional insulator solutions. The results will be compared with experimental breakdown data obtained previously in this program. As a means of alleviating adverse effects of current concentrations, we are investigating the use of rod-type electrodes. Measurements have been made of the resulting additional channel pressure drop and calculations of current distributions have been performed.

The peg-wall test section of the six-Tesla disk generator has been successfully tested under full thermal and electrical conditions. The electrical data from the previous linear channel experiment at high magnetic fields are being analyzed using both one- and two-dimensional models.

TABLE OF CONTENTS

LIST OF FIGURES

1.0 INTRODUCTION

This report describes progress and results for the most recent quarter of the research program, "A High Magnetic Field MHD Generator Program," conducted by the High Temperature Gasdynamics Laboratory at Stanford University under Contract DE-AC01-80-ET15611 with the Department of Energy. The program is directed to a number of important problems in the development of MHD generator channels. The research is primarily experimental in nature, with the use of advanced diagnostics methods and coordinated theoretical and numerical studies for the interpretation of the data and application of the results to large-scale generators. It is intended to provide supporting research for MHD hardware development in areas where performance limitations and design constraints are not now adequately understood.

The research program is divided into three major areas:

Work Area I - Plasma nonuniformities and instabilities
Work Area II - Boundary layer and Hall field phenomena
Work Area III - Six Tesla magnet investigations.

Work Area I involves the effects on generator performance of nonuniformities, including those caused by acoustic and other waves in the MHD channel. Progress in an experimental program to measure the performance effects of controlled nonuniformities introduced in the MHD generator plasma is described in Section 2.0. Present results of an analytic and experimental study of magneto-acoustic waves and their growth and attenuation rates as a function of generator conditions and magnetic field are also reported in this section.

In Work Area II, the development and testing of an improved laser doppler anemometer for the measurement of turbulence damping and resultant effects on MHD boundary layers are discussed in Section 3.0. Results of studies of insulator and plasma induced Hall field breakdown are presented in Section 4.0.

An existing 6 Tesla superconducting magnet has been used in Work Area III for small-scale experiments at high magnetic fields. Progress in the study of both linear and disk generators at high magnetic fields is reported in Section 5.0.

2.0 PLASMA NONUNIFORMITIES AND INSTABILITIES

2.1 Nonuniformity Investigation

An experimental investigation of the effects of nonuniformities in the core of an MHD plasma on overall generator electrical performance continues at Stanford. Local nonuniformities in the plasma electrical transport properties (electrical conductivity and Hall parameter) may arise from incomplete combustion, uneven seed species distribution or from contact with cold flowtrain components. The intent of the experimental investigation is to measure effective channel performance with an induced core nonuniformity and thereby infer losses arising from this mechanism in power-plant scale MHD generators.

2.1.1 Experimental Setup

An experiment was completed in July which combined a diagnostic for measuring plasma temperature profiles and a nitrogen injection apparatus for producing a core nonuniformity in the M-2 flowtrain. Shown in Fig. 2-1 is a schematic of the flowtrain and diagnostic from an overhead view. The Stanford 2.7 Tesla copper-coil magnet was an integral part of the optical setup in that sections were withdrawn from the magnet pole pieces to allow optical access to the M-2 channel ports.

The temperature diagnostic has been described previously [2.1], but a brief review is presented here. Six photodetectors alternately view radiation from the plasma alone and from the plasma plus a reference lamp by means of a chopper. The radiation is resolved spectrally by a narrow-band (10 Å FWHM) interference filter centered near the K D-line at 766.5 nm. The solid angle of radiation incident on the detectors is determined by an aperture stop. By comparing the alternating signals from each photodetector, Kirchoff's law and the assumption of local thermodynamic equilibrium in the plasma core allow a line-of-sight averaged temperature to be calculated [2.1] for each of the six photodetector image locations in the plasma. The six temperature measurements are made transverse to the plasma flow direction at some distance downstream of the nitrogen injection apparatus. For the recently completed test, this distance was approximately 51 cm. (20 in.).

The nitrogen injection apparatus has been described in previous reports [2.2], but a brief review is presented here. A schematic of the injection

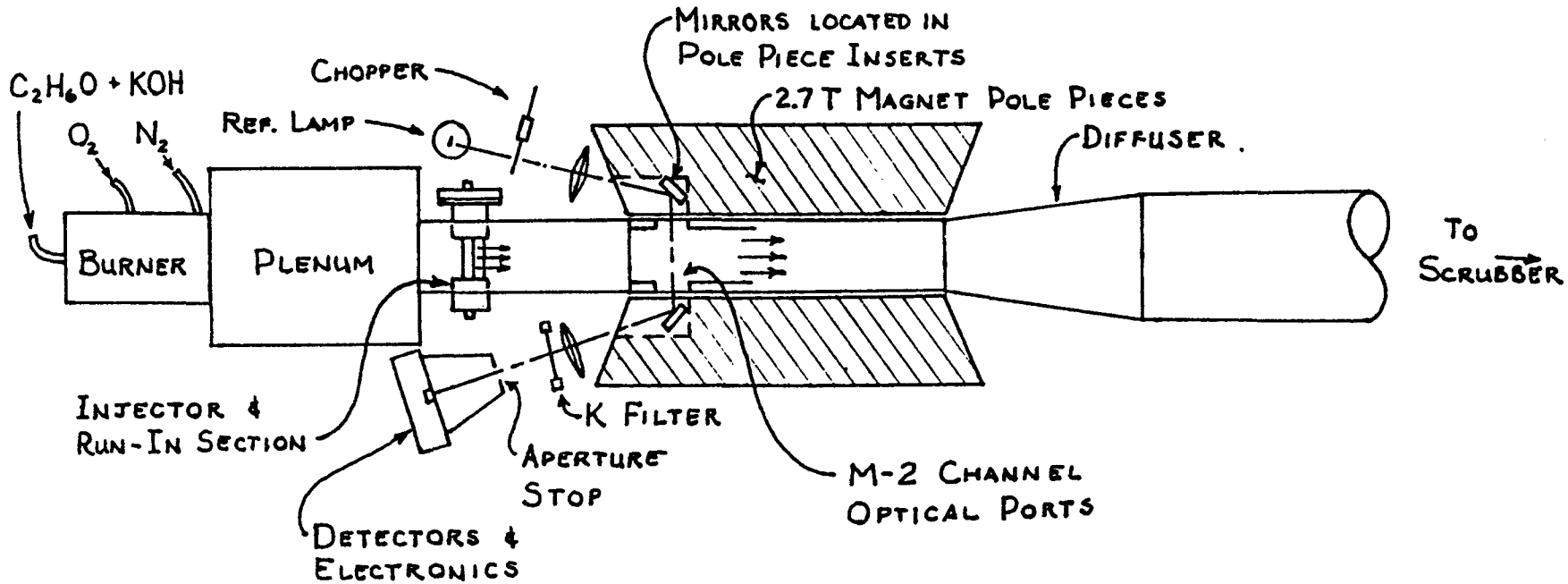

Figure 2-1. Test schematic for injector-diagnostic components (IDC) test series.

apparatus is shown in Fig. 2-2. The injector consists of a water cooled tube 1.6 cm. (5/8 in.) in diameter, a rectangular passage to conduct the injected gas to the ports and a trailing fin, also water cooled. The injector body is constructed of SS304 and the components are brazed together. At either end of the injector body is brazed a copper manifold which provides access to the cooling water and injection gas. The injector is secured across the channel at mid-height by flanged ports in the channel sidewalls. Gas-tight seals are established on the copper manifold surfaces to prevent entrainment of room air into the channel.

Gas is injected into the channel along the injector body through 40 access ports located above and below the trailing fin. The water cooling of the injector body makes it possible to turn the injected gas on and off at will during an experiment. In previous tests [2.2], the injector apparatus has withstood in excess of 10 hours of exposure to plasma at temperatures up to 2700K and leading edge heat fluxes estimated at approximately 400 W/cm^2.

The flowtrain for this test consisted of the M-2 burner, plenum, run-in section and test section, with associated diffuser and scrubber ducting.

The channel inside cross-section was about 10 cm. (4 in.) high by 3 cm. (1.25 in.) wide. The flow conditions included total mass flow rates (not accounting for injection mass flows) of 0.113 kg/sec. (0.25 lbm/sec.), 0.181 kg/sec. (0.40 lbm/sec.), and 0.227 kg/sec. (0.5 lbm/sec.). These mass flows consisted of ethanol premixed with KOH seed material, stoichiometric oxygen and varying amounts of nitrogen, which was used as a diluent to control plasma temperatures.

Nitrogen used for producing the induced nonuniformity was obtained from the building supply with a maximum line pressure of 120 psig (828 kPa). Mass flows of nitrogen through the injector ranged from about 3 to 6 gm/sec.

Measurements for the test included T readings for most flowtrain component cooling water lines, time-varying signals from the six photodetectors and synchronizing signals which allowed demodulation of the detector outputs. Readings were also made of cooling water pressures and delivery pressure of nitrogen to the injector. No electrical measurements were made in this test. The 2.7T magnet was activated during the test to observe the effect of a strong magnetic field on the photodetector signals.

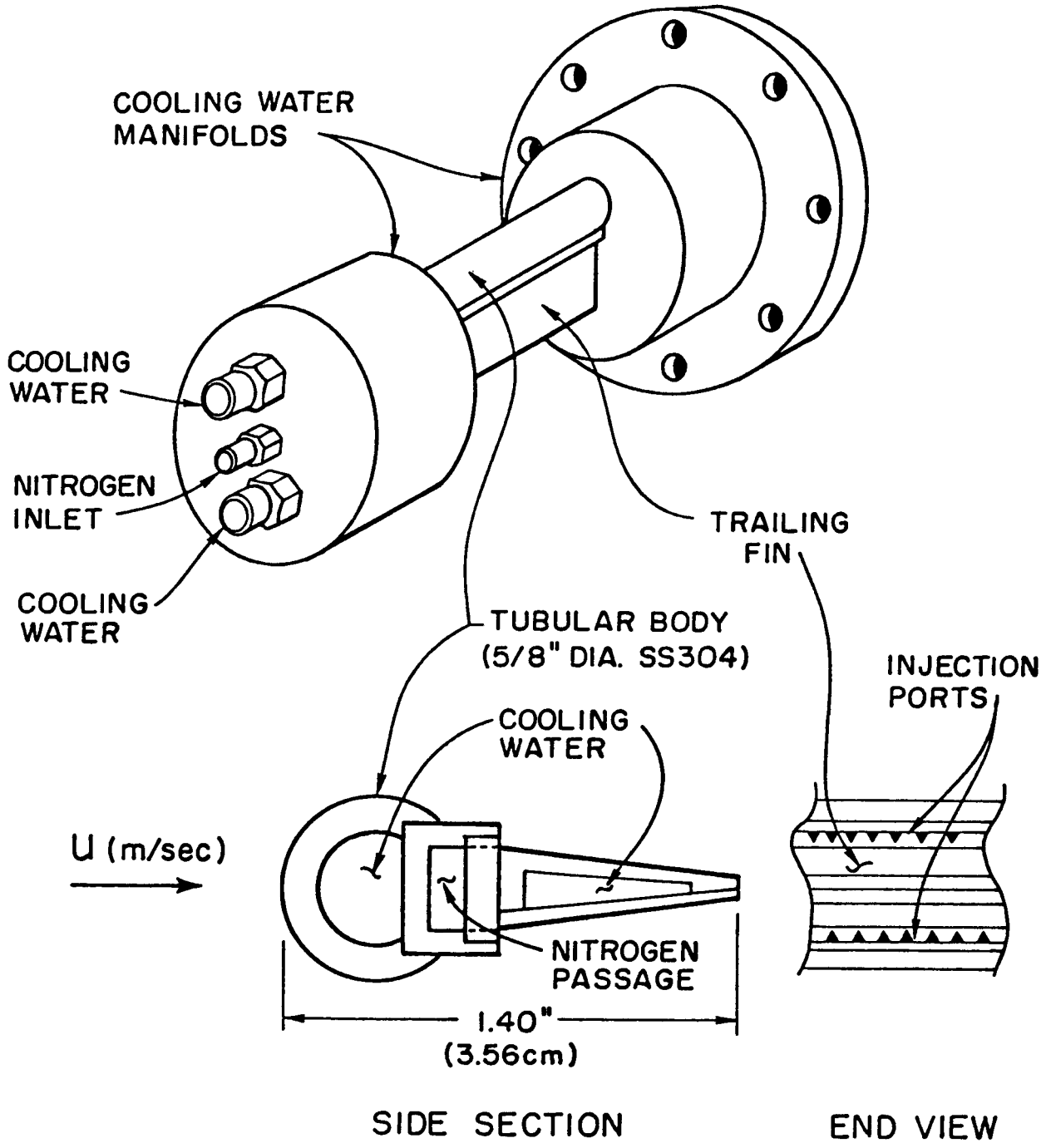

Figure 2-2. Injection apparatus final design.

2.1.2 Experimental Results

Shown in Figs. 2-3 and 2-4 are temperature profiles measured at two run conditions with and without the induced nonuniformity. These data are typical and are referenced to the channel centerline since only half the channel height was observed. The locations of the detector image points were designed to determine the edge of the streamer-like induced nonuniformity and thereby deduce the full-channel structure by assuming symmetry about the channel centerline. The detector image points were about 2.5 mm (0.1 in.) in diameter and were separated by approximately 7.6 mm (0.3 in.).

Equilibrium calculations involving the known reactants and heat losses from flowtrain components allowed an estimate to be made of the plasma temperature. These temperatures are shown in Figs. 2-3 and 2-4 as dashed lines.

It can be seen from these figures that the agreement between equilibrium estimates and measured plasma temperatures with no injection was good, being within about ± 1% typically. Agreement from one measurement to another is good, being typically less than ± 1%. The temperature data reported are results of averaging measurements over a one second period.

It can also be seen that the effect of injecting nitrogen at channel mid-height was to cause a centerline temperature defect of between 40 and 60K at a location 51 cm. (20 in.) downstream of the injector.

2.1.3 Discussion and Modeling

Because of the uncertainty in the data, it was difficult to determine accurately the centerline temperature defect caused by the nitrogen injection. The centerline defect was less than anticipated using 2-D calculations of the diffusion of a temperature perturbation. [2.2]

These results are thought to be attributable to higher turbulent mixing experienced near the channel entrance. In the configuration shown in Fig. 2-1, the injector apparatus is about 6 inches (15 cm.) downstream of the plenum exit. At the transition between plenum and run-in sections, the flow passage is reduced to channel dimensions by a nozzle cut from the refractory ceramic used to line the inner walls of the flowtrain components. Introduction of the nonuniformity in the near proximity of the complex flow

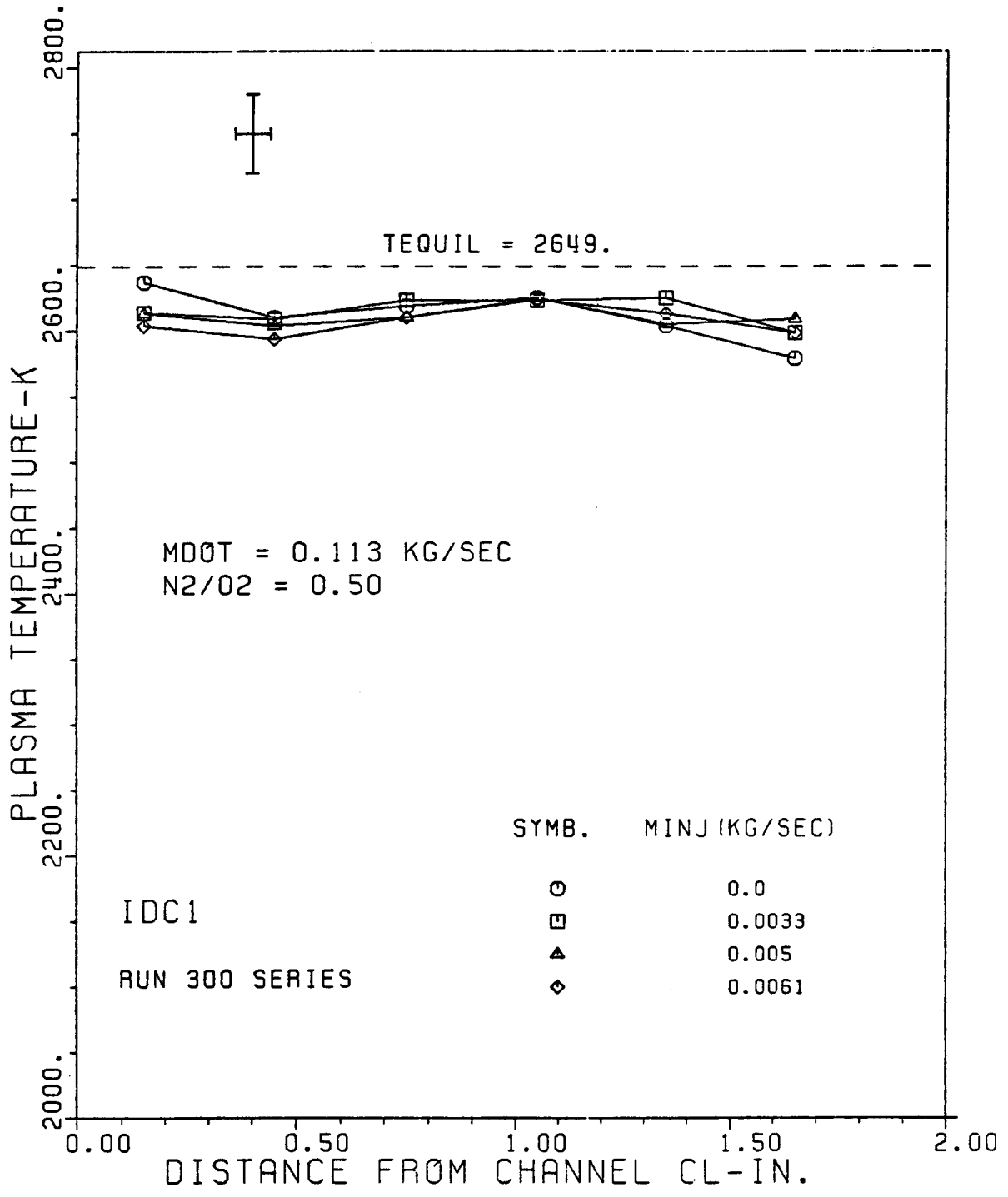

Figure 2-3. Temperature profiles at measurement location for various injection mass flows.

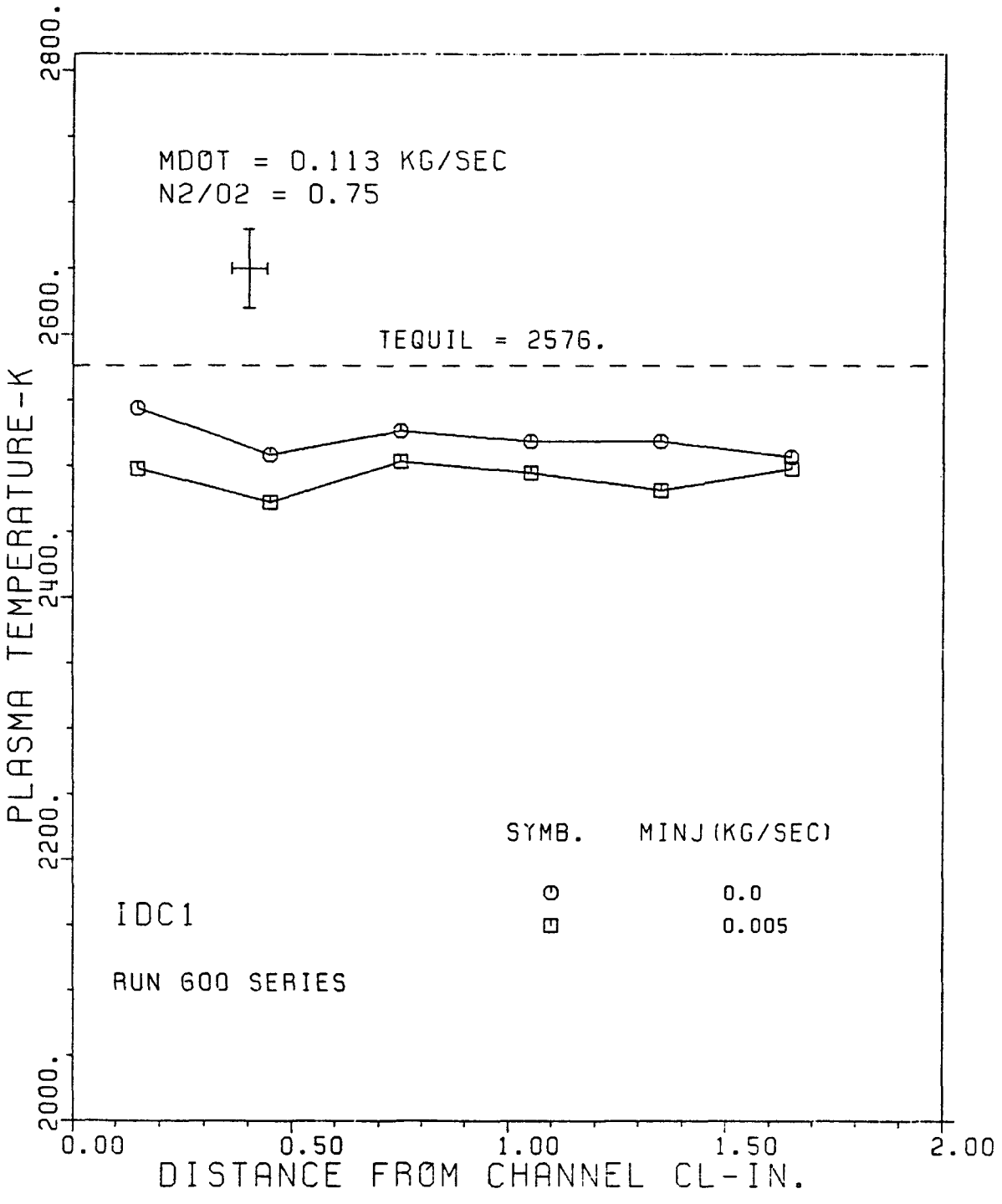

Figure 2-4. Temperature profiles at measurement location for injection $\dot{m}$ = 0.0, 5.0 g/sec.

patterns associated with the channel entrance was thought to result in a rapid diffusion of the nonuniformity structure.

In order to understand the implications of these test results for upcoming electrical experiments, a 2-D plasma model was formulated. In this model, local variations in temperature are assumed to be due to the presence of more or less nitrogen in the gas mixture at that location. The variations in plasma composition are attributed to the diffusion of the induced nonuniformity across the channel as it is convected with the mainstream. The local electrical conductivity may be calculated from equilibrium considerations if the temperature and composition are known. By assuming an initial perturbation in the form of step decrease, say, at the injector location in an otherwise uniform temperature distribution, the diffusion equation may be solved in two dimensions and the entire downstream temperature field generated. From this temperature field the electrical conductivity field may be calculated.

The quantity of interest in these calculations is the resistance measured across the channel in the Faraday direction. Cross-channel averages of transport properties may be calculated at each location in the streamwise direction. These averages, which vary along the channel length, may be used in Rosa's analysis [2.3] of a layered plasma to yield a quasi-2D estimate of the effects of nonuniformities. Oliver's formulation [2.4] of Rosa's results is particularly suited to the calculation of the cross-channel resistance, R_t.

A convenient way to view the result of these calculations is to normalize the resistance at every streamwise location to the cross-channel resistance calculated at a section upstream of the temperature perturbation. Values of this normalized resistance, called $\bar{R}$, which are greater than one give an estimate of the fractional effect of the perturbation (or nonuniformity) at each streamwise location.

This 2-D calculation was compared to the test results to obtain an estimate of the magnitude of effect which could be expected in an electrical test. A step decrease in the temperature distribution at the injector location was used to model the induced nonuniformity. The nonuniformity was assumed to introduce a room temperature gas at the injector location. The width of the step was determined from energy balance considerations. The turbulent diffusion coefficient was varied until the temperature distribution

at the measurement location 51 cm. (20 in.) downstream approximately matched the experimental data. The result of one such calculation is shown as the top graph in Fig. 2-5. The family of four curves shows the temperature profile at the channel entrance (XD = 0.00 cm.), the introduction of the step perturbation (XD = 7.50 cm.), the halfway point between the perturbation and the measurement location (XD = 29 cm.) and the measurement location (XD = 66 cm.). The corresponding electrical conductivity profile is shown on the right side of the same figure for the same locations. Both profiles stop at a distance of 6 mm from the channel wall, where boundary layer effects are assumed important. The flow conditions for Fig. 2-5 are the same as for those in Fig 2-3. Temperature data for the maximum nitrogen injection case are designated by symbols.

The bottom graph in Fig. 2-5 shows the cross-channel resistance in Ohms and the normalized resistance as a function of the streamwise coordinate. The total cross-channel resistance is calculated by combining the core average calculated using the Rosa model and the resistance expected in the boundary layers. These boundary layer resistances are obtained from experimental voltage drop measurements in the M-2 channel under run conditions similar to those assumed in the calculation [2.5]. The results shown in Fig. 2-5 are for no magnetic field.

It can be seen in the graph of normalized resistance that the effect of the step decrease in temperature is quite large near its origin, but decays rapidly. The net effect at the measurement location is seen to be only about 0.5%. The diffusion coefficient used in the calculations of Fig. 2-5 was 1.0 m^2-sec. Larger values of this coefficient produced virtually no change in the normalized resistance calculated at the measurement location. Simple order-of-magnitude arguments for the diffusion coefficient suggest that values near 0.8 m^2-sec. are reasonable for these flow conditions.

The result of these calculations suggest a need for much larger perturbations in the temperature field in order to produce an effect which will be sustained along the length of the channel. It was thought that in order to accurately resolve the effect of the induced nonuniformity in the channel, a 15% increase in the cross-channel resistance would be necessary. More calculations were performed for the same run conditions as Fig. 2-5 but with the

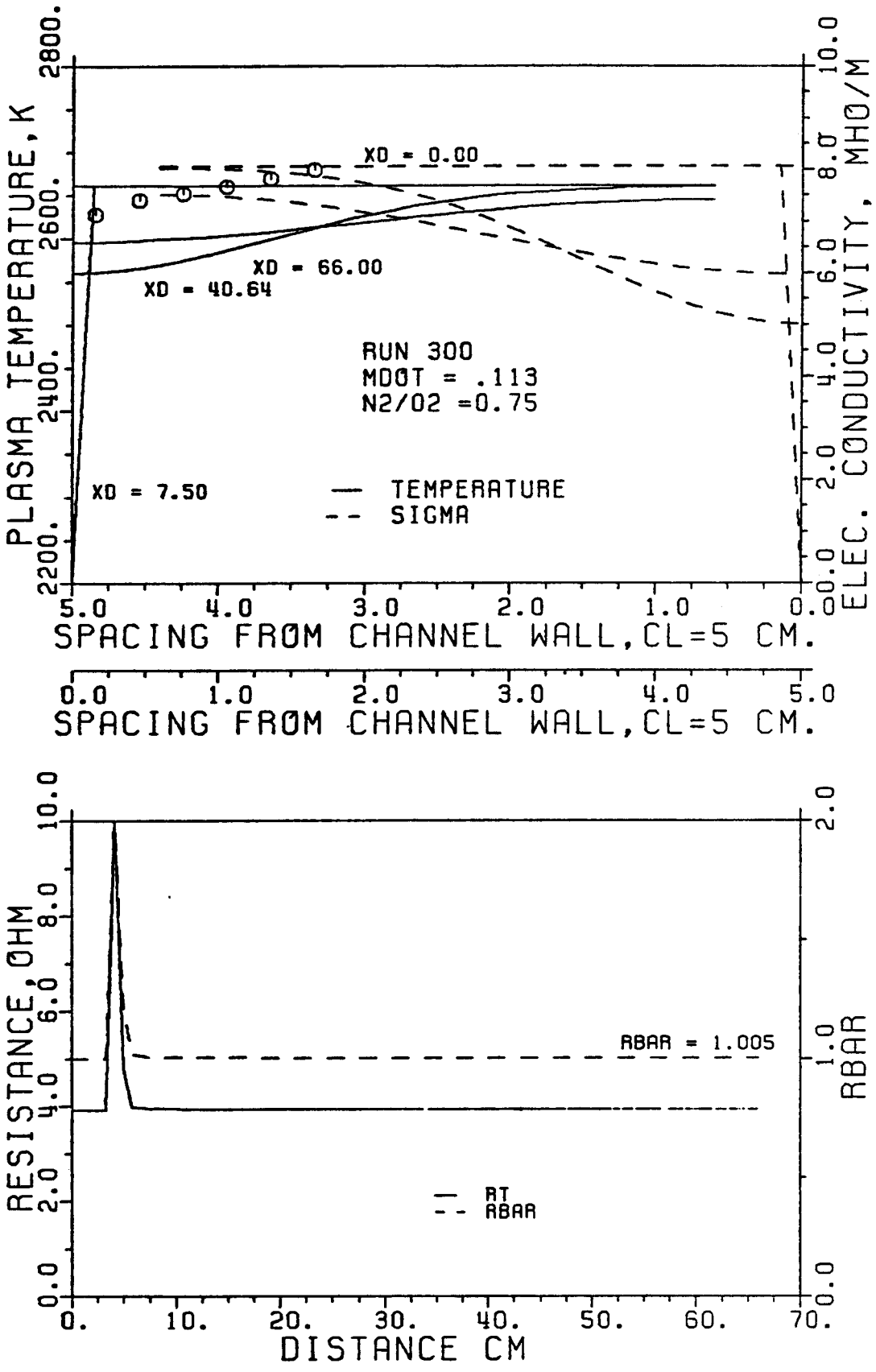

Figure 2-5. Two-dimensional diffusion of a temperature perturbation and resulting cross-channel resistance.

width of the step perturbation increased, which corresponds to higher injection mass flow rate.

The results of one such calculation appears in Fig. 2-6. The increase in $\bar{R}$ is seen to be more sustained for this case as compared to Fig. 2-5, with the result of a 12% effect at the measurement location. Energy balance considerations allow the calculation of the mass flow rate of room-temperature nitrogen required to produce this magnitude of effect. It was found that, for these flow conditions, an injection rate of about 20 gm/sec. would be necessary as compared to the ~ 6 gm/sec. flow rate of the previous test.

A higher injection rate would be needed to produce a similar effect in a higher total mass flow plasma. Such a plasma would be needed to approximate actual generator conditions in our MHD flow train. A worst-case calculation would then include a large total mass flow run condition.

In Fig. 2-7 are shown the results of calculations for a total mass flow of 0.272 kg/sec. (0.6 lbm/sec.) and a N_2/O_2 mass ratio of 0.5, which yields a plasma at about 800 m/sec. and 2730K. An approximately 19% increase in the cross-channel resistance can be achieved, it is estimated, if ~ 50 gm/sec. of room temperature gas could be injected into such a flow, for a mass injection which is about 16% of the total flow rate.

2.1.4 Future Experiments

The results of the previous experiment and the 2-D calculations suggest that, in order to produce the magnitude of effect desired, significantly higher injection mass flows will be required than suggested by earlier, 1-D models. This is thought to be due to higher turbulent mixing at the channel entrance than anticipiated and to two-dimensional effects which were not included in earlier calculations of the cross-channel resistance.

A series of experiments are being planned in which the injector and temperature diagnostic will be used in conjunction with electrical measurements both with and without applied E- and B-fields. In this series of experiments, the M-2 channel will be reversed end-for-end to allow temperature measurements downstream of the 2.7T magnet active region.

Two steps will be taken to enhance the effects of the induced nonuniformity. The injector apparatus will first be moved approximately 18 inches

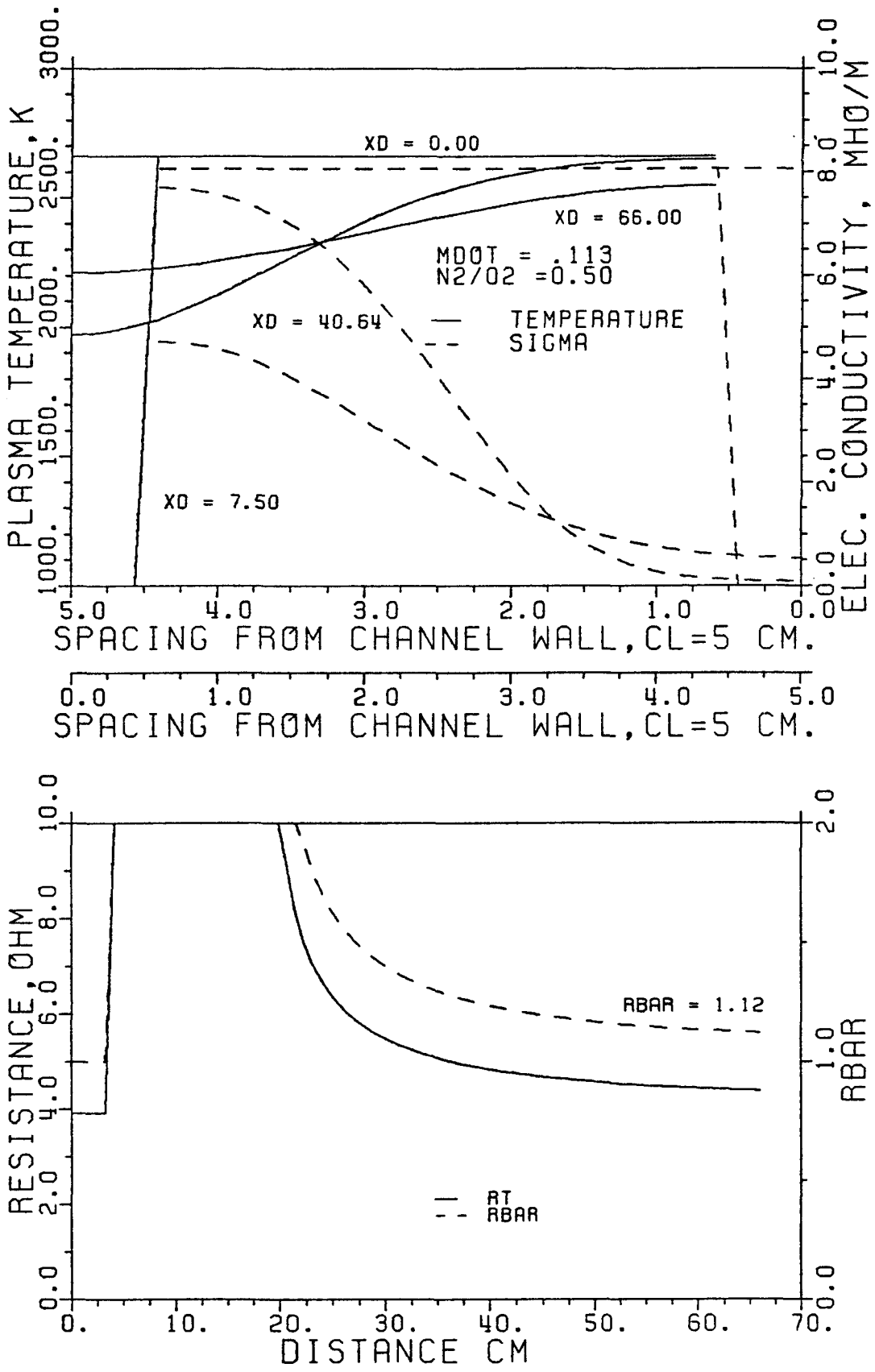

Figure 2-6. Two-dimensional calculation for ~ 12% effect at measurement location (XD = 66 cm.)

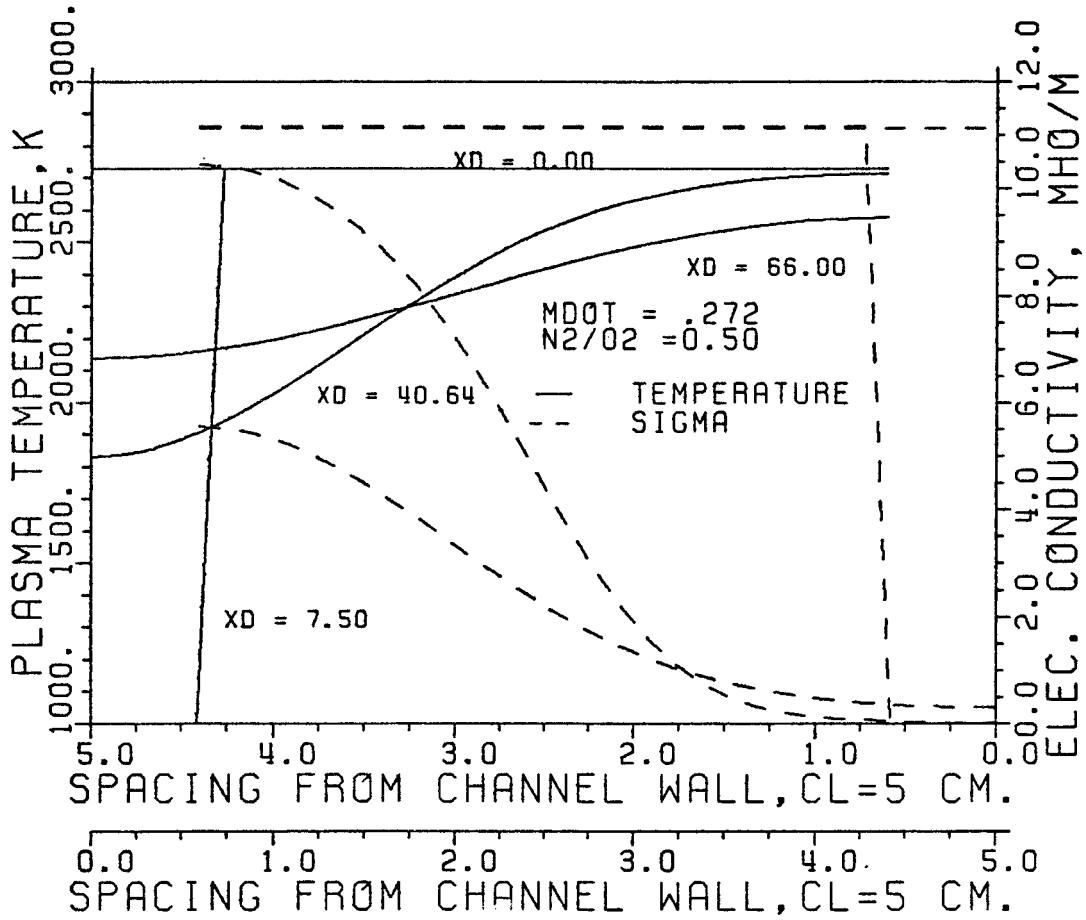

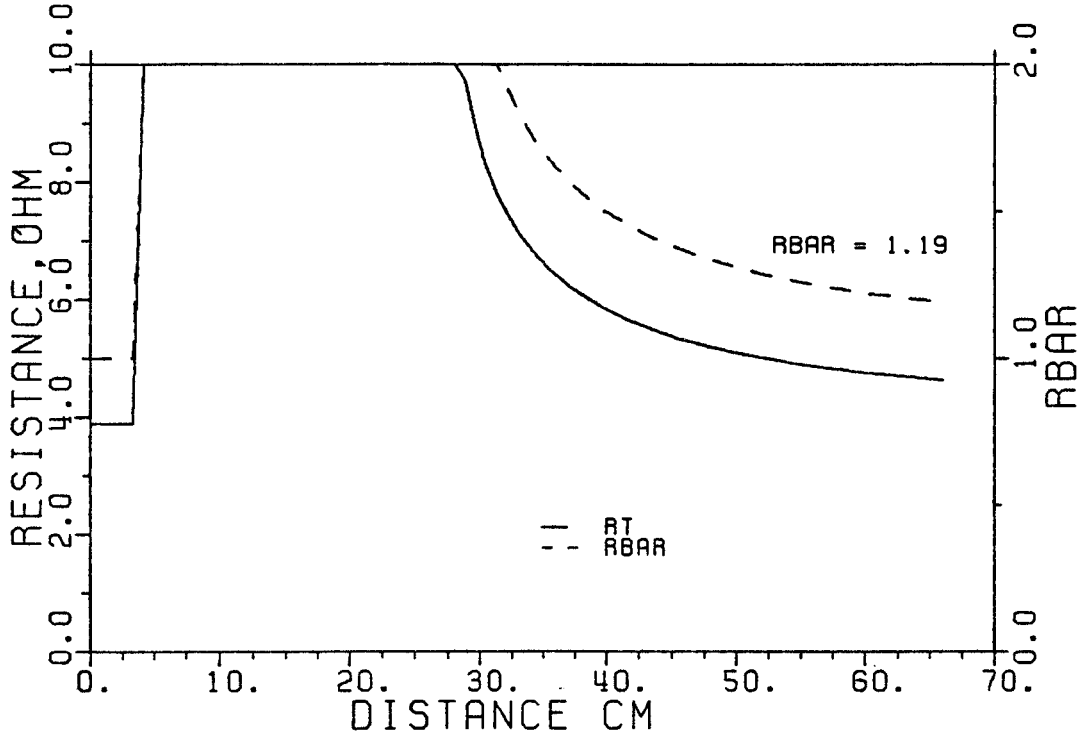

Figure 2-7. Two-dimensional calculation for initial mass flow rate of 0.272 kg/sec.

(46 cm.) downstream from its position as indicated in Fig. 2-1 by; 1) reversing the present run-in section end-for-end and 2) including another run-in section upstream of the present one. This move will cause the overall plasma temperature to be somewhat lower due to heat loss, but it should allow the nonuniformity to be introduced in a relatively calmer section of the flow. The second step will be to modify the injector apparatus itself by enlarging the injection ports through which the room-temperature nitrogen must pass. This will allow higher injection mass flow rates for the same delivery pressure to the apparatus.

The electrical test series is presently expected to begin in October. Measurements will be made over a range of flow conditions, injection flow rates and electrical loads. It is expected the test apparatus will also be used in the Faraday, diagonal and Hall configurations and over a range of Hall parameters.

The results from this test series are expected to allow a relationship to be determined between the apparatus electrical behavior and the local plasma transport properties in the form of an effective Ohm's law. Once this relationship is established with some confidence, the effective Ohm's law may be written for a large-scale MHD generator and performance levels predicted in the presence of core plasma nonuniformities of the type studied here.

2.2 Magneto-acoustic Disturbances

In the area of magneto-acoustic disturbances, a major experiment in the M-2 facility to study the formation and behavior of propagating waves in a combustion MHD generator was completed. The principal purposes of the test were two-fold. The first objective was to measure the effects of magnetic field and current on single disturbances which pass through the MHD channel as acoustic and entropy waves. Models developed at the HTGL [2.6 - 2.7] which include non-ideal generator effects such as boundary layer and near electrode phenomena predict that the entropy (temperature) waves, propagating at the core fluid velocity, might experience small, but observable, amounts of attenuation in the Stanford facility. The experimental observations of wave growth rates would support or improve a similar model for magneto-acoustic disturbances which suggests that significant amplification of acoustic disturbances could occur in proposed large-scale MHD generators, if electrical

resistances in the electrode wall boundary layers are not too large. The second objective was to measure the shape and magnitude of propagating acoustic and entropy waves created by a rapid current discharge between a pair of Faraday electrodes. The measurements and a model for the wave formation [2.8] identify important interaction between the flowing plasma, current and magnetic field, and provide a description of a useful and convenient experimental technique which can be used in other MHD facilities to create controlled disturbances of the plasma pressure and temperature. For both the wave growth and wave shape measurements a special high-speed digital data acquisition system was assembled which permitted high frequency resolution of the rapidly propagating waves. Data reduction is underway and an analysis of the experimental data will be presented in a forthcoming report.

Data was acquired during ten hours of MHD channel operation on two separate days at mass flow rates betwen .068 and .113 kg/sec (Mach number .16 to .27) with nominal plasma core temperatures of approximately 2800 K. Electrical conductivity of the plasma was 10-15 mhos/m. Current densities varied between zero (open circuit) and 1.25 A/cm^2, at magnetic field strengths between zero and 2.5 Tesla. Instrumentation of the channel allowed measurement of the steady-state thermal and electrical performance of the channel, and high frequency measurements of the transient waves. Steady-state data includes Faraday and Hall voltages, Faraday currents, potential on transverse mounted voltage pins, electrode temperatures, and the reactant flow rates. Transient measurements were taken at three locations along the MHD generator within the area of magnetic field, which correspond approximately to the locations of the first, last, and central electrode pairs. At each location were a probe-tube microphone [2.9] to measure local pressure fluctuations, a fiber optic luminosity probe for sensitive relative temperature fluctuation measurements, and transverse voltage pins to measure local core voltage fluctuations. In addition, special current shunts in the nearby electrodes provided a measurement of Faraday current fluctuations. Thus, time dependent pressure, temperature, voltage and current data could be obtained at each location, and give a record of the evolution a propagating wave as it passed through the MHD channel. Each device had a bandwidth of over 50 kHz, excepting the probe-tube microphones which attenuate the signal by 10-15 db at 25 kHz, but have a known response function.

Single propagating waves were created by discharging a large capacitor in the plasma through a pair of electrodes. The time constant of the discharge was approximately 150 sec, creating waves of 0.5 - 1.0 msec in duration. By varying the voltage of the discharge, pressure pulses up to 20 kPa and temperature pulses of approximately 150 K were obtained, which are well above the inherent background fluctuation levels. Each discharge produced three distinct travelling waves - an upstream and a downstream moving acoustic wave, each moving at the sonic velocity with respect to the moving plasma, and an entropy wave moving at the plasma velocity. The voltage and current of the discharge could also be recorded, to obtain information about the wave formation process. As utilized, the probe-tube microphones have a sensitivity of 5 Pa (smallest bit of A/D Converter). The relative luminosity measurements are extremely sensitive, can resolve temperature fluctuations of approximately 1.5 K in the entropy waves and about .5 K in the acoustic waves.

Some combination of these signals and the other transient measurement were sampled by an analog to digital converter at a 500 kHz total data rate (50 kHz per channel) and stored on magnetic tape for post-test analysis. When desired, on-line video display of the pulse data was possible.

For the measurements of wave growth rates, waves were created upstream of the MHD generator section and allowed to propagate into the region of magnetic interaction. The faster downstream moving acoustic wave preceded the slower entropy wave into the channel. Comparison of the amplitudes of the travelling pressure and temperature waves at the entrance and exit of the generator section will show the effect of magnetic interaction on a wave during one pass through the channel. Because the analytical model of the interaction predicts only a small change in wave amplitude, many wave signals (typically 50 to 100) are compared at each run condition, in order to find a statistical trend in the amplitude variation of the waves with increased magnetic interaction.

The formation of wave pulse shapes was studied by discharging the capacitor inside the magnetic field at open circuit conditions and measuring the wave shapes as they propagated out of the channel in both upstream and downstream directions. Additional current and voltage measurements of the discharge provided knowledge of the conditions which created the waves. Previous modelling and measurements [loc. cit. 2-8] showed that a current discharge normal to both the direction of flow and the magnetic field acts on

the plasma to create travelling waves through two mechanisms. First, a J x B body force acts in the direction of flow (or opposite to the flow, depending on the sign of J) to create a rarefied acoustic wave travelling in one direction and a compressive acoustic wave travelling in the opposite direction. At the same time, Joule heating causes the gas to expand, creating compressive acoustic waves travelling in both directions, and an entropy (or temperature) wave which is convected downstream with the flow. This Joule heating effect exists, independent of the value of the magnetic field. The two effects combine to produce a stronger compressive acoustic wave in one direction, and in the opposite direction a weaker wave, either compressive or rarefied, or no wave at all, depending upon the magnitude of the current and magnetic field strength. Initial examination of the new data, taken at several values of magnetic field and at different levels of current discharge, strongly supports these conjectures.

Because of the short event times associated with the travelling waves, a special high speed data acquisition system was utilized in order to obtain good temporal resolution of the transient phenomena. An acoustic wave passes through the channel in approximately 0.5 msec, while an entropy waves travels through in about 2.5 msec. A schematic representation of the high-speed data acquisition system is shown in Fig. 2-8. After flow conditions are established the computer operator initiates the data acquisition sequence, passing control parameters to the A/D converter and preparing memory locations for the data. The operator can then repeatedly charge and fire the capacitor. When the discharge command is issued, internal circuitry in the capacitor discharge system signals the time delay trigger. After a short time delay, the trigger activates the multiplexer which initiates data conversion. The time delay is adjusted so that data conversion can begin in advance of the current discharge which creates the wave disturbances. Anti-aliasing filters condition the analog data signals before digitization. A typical block of data from a single pulse consists of ten arrays (ten channels) of 512 data points, where each channel is scanned at 20 sec intervals for a total data rate of 500 kHz. After some signal processing the data can be displayed on video monitors and written to magnetic tape for post-test analysis. Data blocks are taken repeatedly until an on-line display of statistical parameters, calculated from the data, indicates stationarity of the signals.

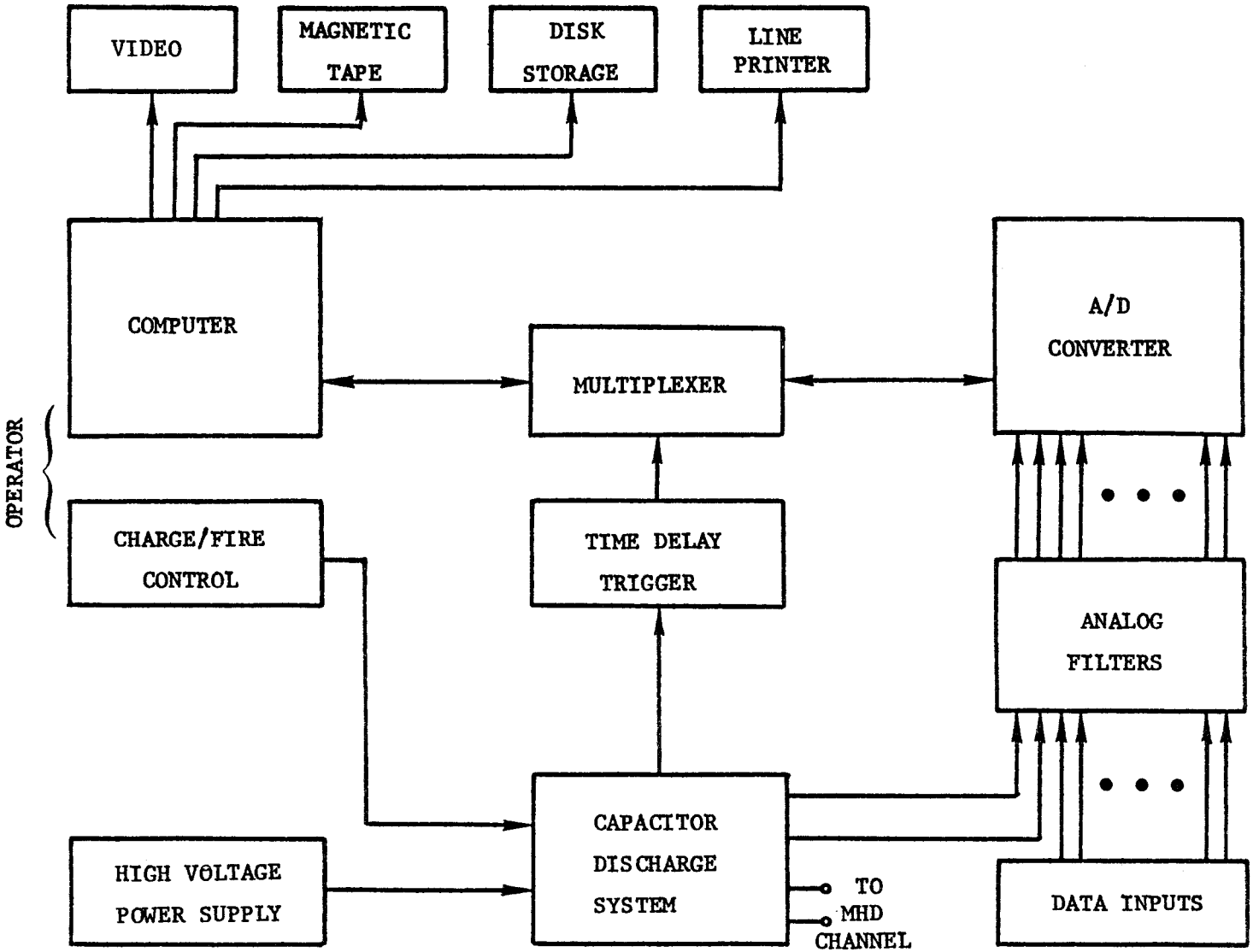

Figure 2-8. High-speed data acquisition and capacitor discharge systems.

Simultaneous, sensitive, high-frequency measurement of pressure, temperature, voltage and current fluctuations associated with propagating acoustic and entropy waves were made in a combustion MHD generator under conditions of applied magnetic field (up to 2.5 Tesla) and moderate current density (up to 1.25 A/cm^2). The measurements, which are presently under analysis, provide an experimental data base for the study of plasma instabilities and demonstrate a technique for producing large controlled plasma disturbances.

3.0 BOUNDARY LAYER PHENOMENA

3.1 Overview of the Present Boundary Layer Program

One of the important phenomena in an MHD generator is the interaction between the hot, flowing plasma and the cooler, stationary walls. This interaction, governed primarily by the hydrodynamic and thermal boundary layers, and by radiative heat transfer, can be important in determining the overall performance and efficiency of the MHD power generation facility. The shape and size of the boundary layers govern the loss mechanisms of pressure drop through skin friction and enthalpy loss through heat transfer to the wall, as well as electrical losses due to the influence of a low temperature, conductivity fluid layer between the electrodes and the core. Because the interaction between the electrical effects and fluid mechanics creates boundary layers substantially different than those of non-MHD flows, much of the work at Stanford is directed toward the measuring and understanding the fluid mechanics of MHD flows. The boundary layer program at Stanford has successfully measured and modeled such phenomena as the velocity overshoot on the insulator wall for extended Hartmann flow [3.1] and Joule heating on the electrode wall [3.2].

The current thrust of the boundary layer program is to measure the influence of the magnetic field on the turbulent flow structures present in MHD channels. Measurements in liquid metals [3.3, 3.4] have shown that the magnetic field suppresses the turbulent eddies, and can laminarize a turbulent flow. This turbulence suppression reduces the turbulent mixing in the boundary layers which reduces the friction and heat transfer losses, thus increasing the efficiency of an MHD power generation facility. Rankin [3.5] included a turbulence suppression model in his research of MHD generators and reported a 12% decrease in the skin friction coefficient and Stanton number for a 250 MW thermal pilot plant.

The effect of turbulence suppression has long been of interest to the MHD program at Stanford. Olin [3.6] made turbulence suppression measurements in a combustion driven MHD plasma using a cooled pitot tube in 1966. Although he was not able to measure the turbulence directly with a pitot tube, he reported a definite trend toward laminarization in the mean velocity profiles. With the development of high-speed digital computers and stable, high-power lasers,

it is now possible to make direct measurements of the turbulence levels in the harsh MHD environment by the use of Laser Doppler Velocimetry (LDV). Although Rankin's main research goals were in other areas, he reported turbulence suppression measurements for one flow condition [3.5]. His results were qualitatively similar to those of Olin, confirming the presence of turbulence suppression in combustion-driven MHD plasmas.

With the availability of state-of-the-art LDV systems, it was decided to make a thorough study of the magnetic suppression of turbulence. Various LDV optical systems were evaluated, and one was selected. After a thorough study of this system, a data acquisition/reduction system was also acquired and the whole system tested on a bench top flow, as well as in an MHD channel. Computer algorithms were selected for post-test statistical analysis of the data. A complete description of this system and algorithms has been provided in previous reports.

3.2 Statistical Analysis of LDV Data

During this reporting period, the main work has been to write the complex statistical analysis computer code that does the post-test analysis of the data. This analysis, based upon the work of Mayo [3.7], includes the construction of an autocorrelation function and power spectral density function from the random time sampled velocity data. The computer code is nearly complete and some preliminary results have been obtained from data taken in previous MHD tests. The code is now undergoing a series of exhaustive tests to correct any errors and to demonstrate its reliability and accuracy. When these tests are completed, the code will then be used as a design tool to help design the final turbulence suppression MHD experiments, as well as to reduce the data taken from the tests. Preliminary analysis of the existing LDV data has shown several ways to significantly improve the accuracy and range of the data to be taken in the final tests. This improvement is possible because of the capability of the computer code to relate statistical information about the MHD flow to system parameters like data rate, total amount of data, and timer settings.

Several of the milestones for the development of the code have already been achieved. The first was to demonstrate that the small computer available is capable of handling the large code and the massive amount of data needed.

The second was to provide the capability of flexible graphical output for the data. The third milestone is related to the validity of the algorithms used. One of the Fourier Integral Theorems states that the integral of the power spectra over all frequencies is equal to the D.C. value of the auto-correlation function, i.e., the turbulence level. Output from the code has shown that the integral of the computed power spectrum is indeed equal to the turbulence level as calculated by standard methods. This result has shown that the basic concept behind the code is valid and that it can be used to compute power spectual density functions for random time sampled LDV data.

Preliminary plots of a velocity probability distribution function, an autocorrelation function, and a power spectral density function are shown in Figs. 3-1, 3-2, and 3-3, respectively. Figure 3-1 shows the expected Gaussian behavior of a velocity probability density function. Figure 3-3, the power spectral density function, is plotted on a linear scale rather than the normal log scale, and the units on the vertical axis are arbitrary: given only to show the relative contributions at the various frequencies. The purpose of these non-standard variations on the plot is to illuminate the structure of the noise apparent in both Figs. 3-2 and 3-3.

A study of the sources of the noise has been made, with the primary source tentatively identified as an insufficient number of data points. A second source is spectual leakage from truncation effects on the autocorrelation function. A benchtop experiment is being designed and the computer code is being modified to test the hypothesis of insufficient data, and various window functions are being studied and applied to reduce spectual leakage. Digi-tation effects in the LDV burst counter, timer, and computer appear not to add a significant amount of noise to the plots.

One of the important issues being studied by researchers of LDV appli-cations is the influence of velocity biasing. This has been discussed in previous reports. A modification to the computer code is being added to compute the cross-correlation function between the data arrival rate and flow velocity. This should provide additional information about what effects velocity biasing may have, if any.

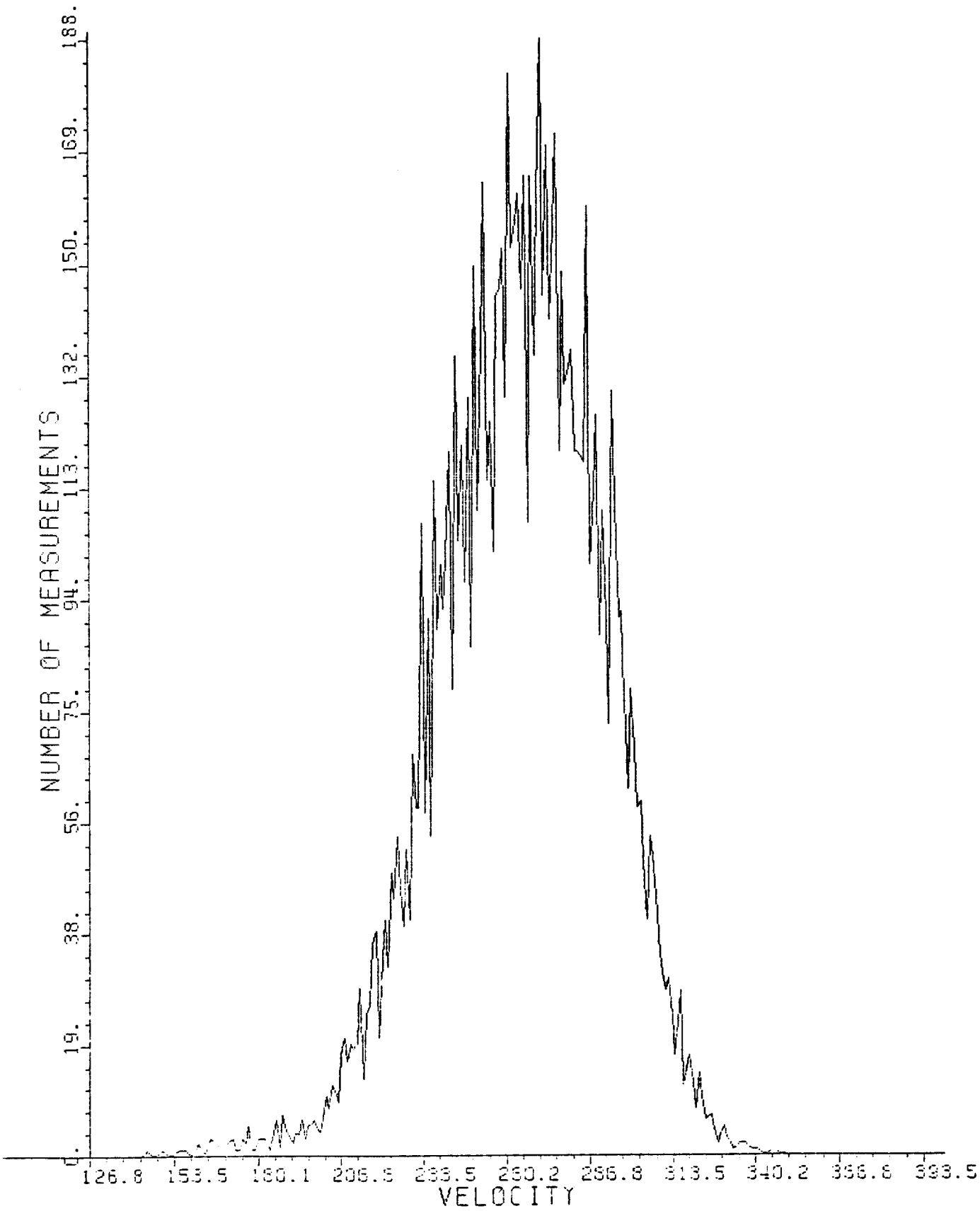

Figure 3-1. Preliminary velocity probability distribution function of MHD data.

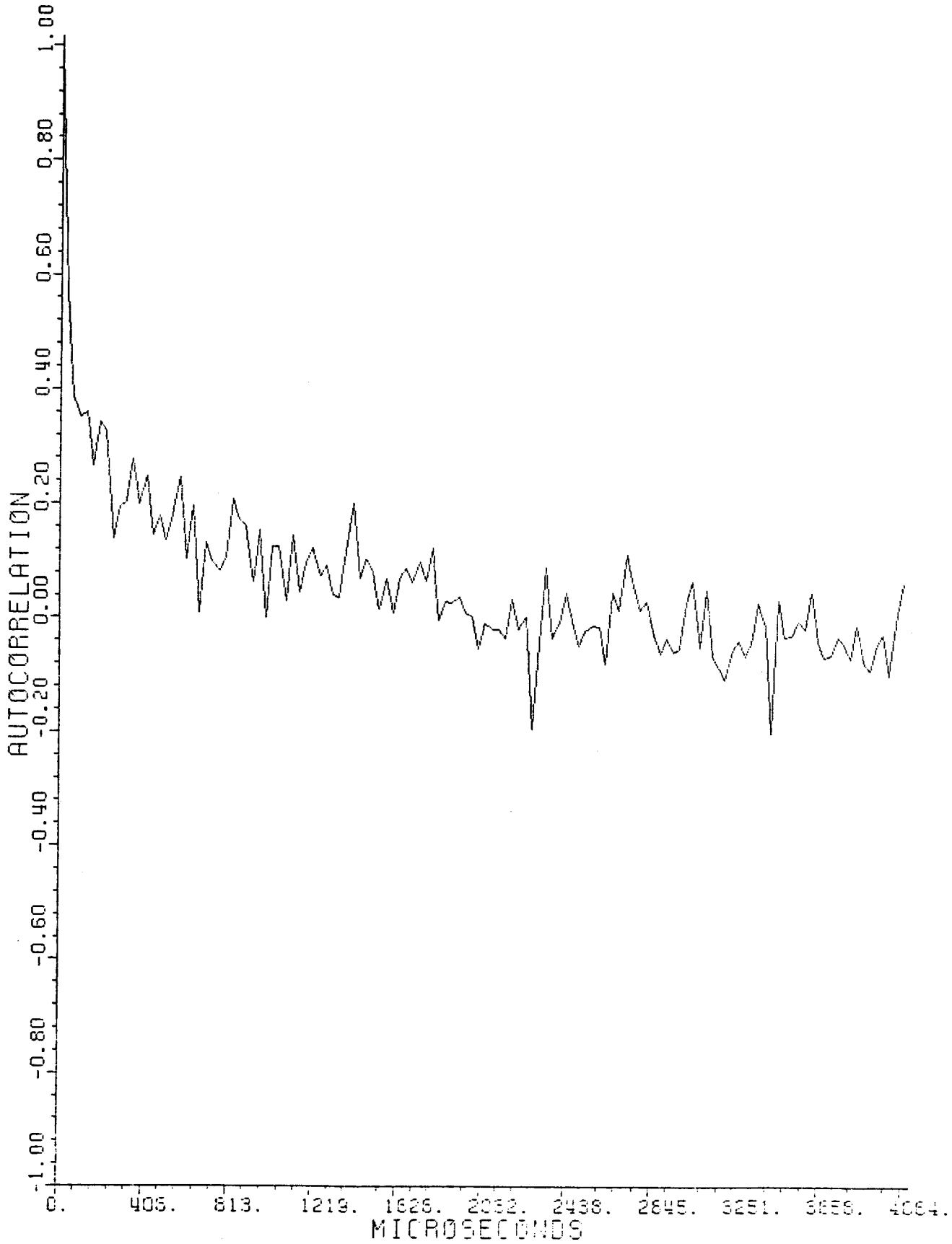

Figure 3-2. Preliminary autocorrelation function of MHD velocity data.

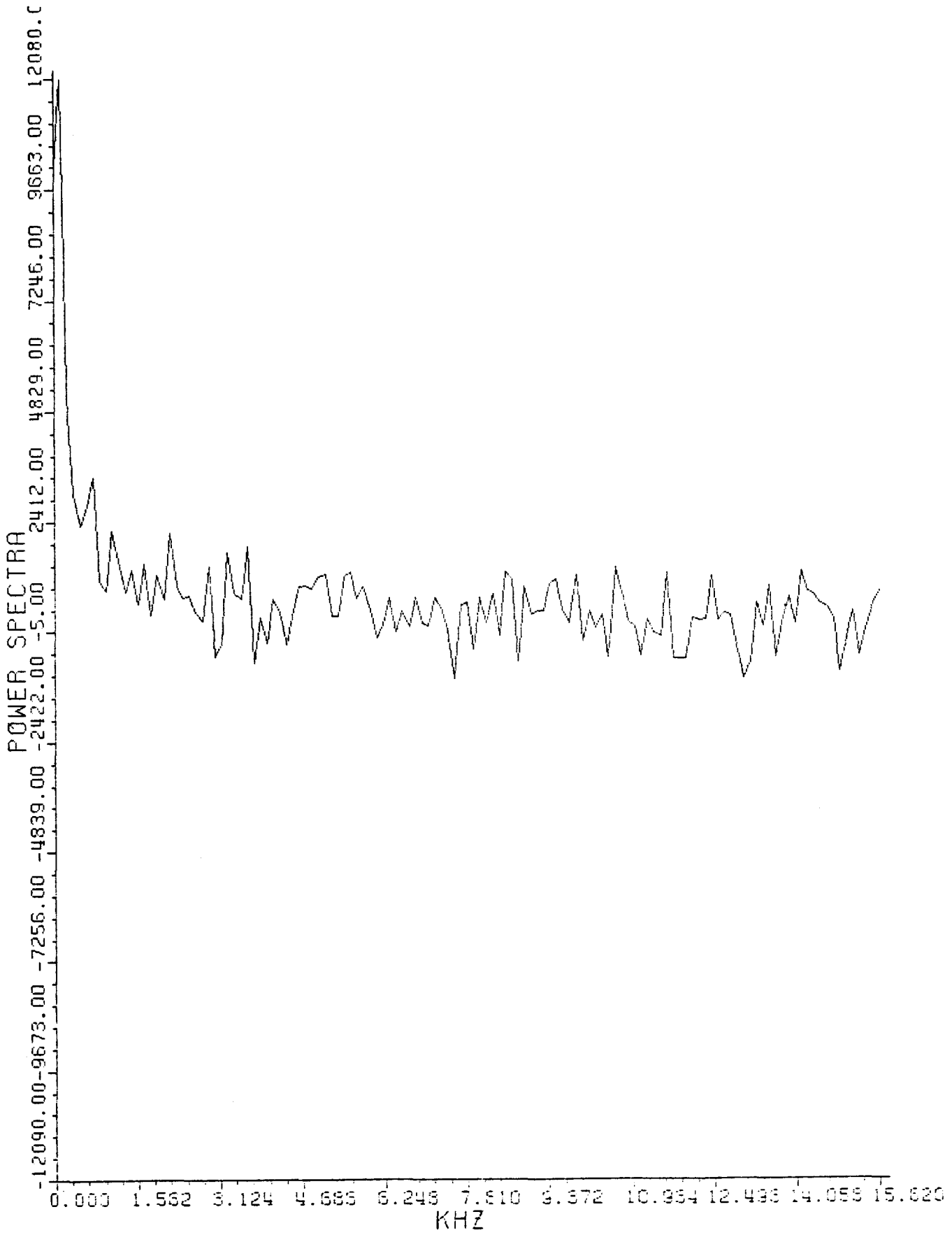

Figure 3-3. Preliminary power spectral density function of MHD velocity data.

4.0 HALL FIELD BREAKDOWN

In the present reporting period, two plasma electrical models and an electron energy model have been developed and incorporated into an existing boundary layer program [4.1]. The electrical models consist of an electrode current concentration plasma electrical model and a plasma current streamline solver. These models perform more detailed calculations than those previously used [4.1], thereby permitting more accurate calculations of the interelectrode plasma and insulator response to an induced axial field.

In Section 4.1, the underlying theory governing the two plasma electrical models will be described. Section 4.2 will present the theory pertaining to the electron energy equation.

4.1.1 Electrode Current Concentration Plasma Electrical Model

The electrode current concentration plasma electrical model is similar in form to the finite element model developed by Oliver. [4.2] In the present model, however, the plasma region adjacent to the electrode is treated in more detail. This permits calculation of the current concentration at the electrode surface. In the following paragraphs the underlying theory and assumptions will be described. Figure 4-1 describes the calculation region.

Two global current conservation equations are enforced in the present model.

$$\int_o^{Le} J_y \, dx \Big|_{y=0} = J_{y\infty} \left(Le + Li\right) \tag{4.1}$$

$$\frac{1}{Li} \int_{Le}^{Le + Li} \left[\int_{-A}^{Yc} J_x \, dy \right] dx = 0 \tag{4.2}$$

Equation 4.1 enforces the requirement that the net current flowing through the electrode surface must equal the net current flowing through the plasma core. Equation (4.2) enforces the condition that the axial average of the net axial current, through the plasma region adjacent to an insulator, and through the corresponding insulator must vanish.

A single global voltage continuity equation is employed in the model.

$$V + IR = -\int_o^{2Y_c} \vec{E} \cdot d\vec{L} = 2V_o - E_{x\infty} L_e - 2 \int_\delta^{Yc} E_{ye}(Le + Li, y) dy \tag{4.3}$$

Equation 4.3 ensures that a line integral of the electric field through the plasma, from one electrode to its Faraday pair, matches the imposed load voltage. The integration assumes that the boundary layer voltage drops at the upper and lower electrodes are antisymmetric reflections of each other. Figure 4.2 indicates the integration path for the above integral.

In addition to global voltage continuity, local voltage continuity is enforced for the electrode boundary layer. This constraint is mathematically imposed by the following relationship.

$$V_\delta(x) = - \int_o^\delta E_{ye}(x,y)dy = V_o - E_{x\infty}\, x \tag{4.4}$$

This equation is applied at every axial location along the electrode, thereby permitting the calculation of the transverse current density at every axial location along the electrode.

The assumed functional forms for the plasma transverse current densities and axial electric fields are identical to those of Oliver with an exception for the transverse current density in the electrode region.

$$J_{ye} = J_{y\infty}\left[\phi(y) + \left(1 + \frac{Li}{Le} + F_{ye}(x)\right)\left(1 - \phi(y)\right)\right] \tag{4.5}$$

$$J_{yi} = J_{y\infty}\,\phi(y) \tag{4.6}$$

$$E_{xe} = E_{x\infty}\,\phi(y) \tag{4.7}$$

$$E_{xi} = E_{x\infty}\left[\phi(y) + \left(1 + \frac{Le}{Li}\right)\left(1 - \phi(y)\right)\right] \tag{4.8}$$

The subscripts i and e refer to the insulator and electrode regions respectively. The remaining axial currents and transverse electric fields are obtained from Ohm's law for the plasma.

$$J_x = \sigma E_x - \beta\, Jy \tag{4.9}$$

$$E_y = uB + \frac{1 + \beta^2}{\sigma} J_y - \beta\, E_x \tag{4.10}$$

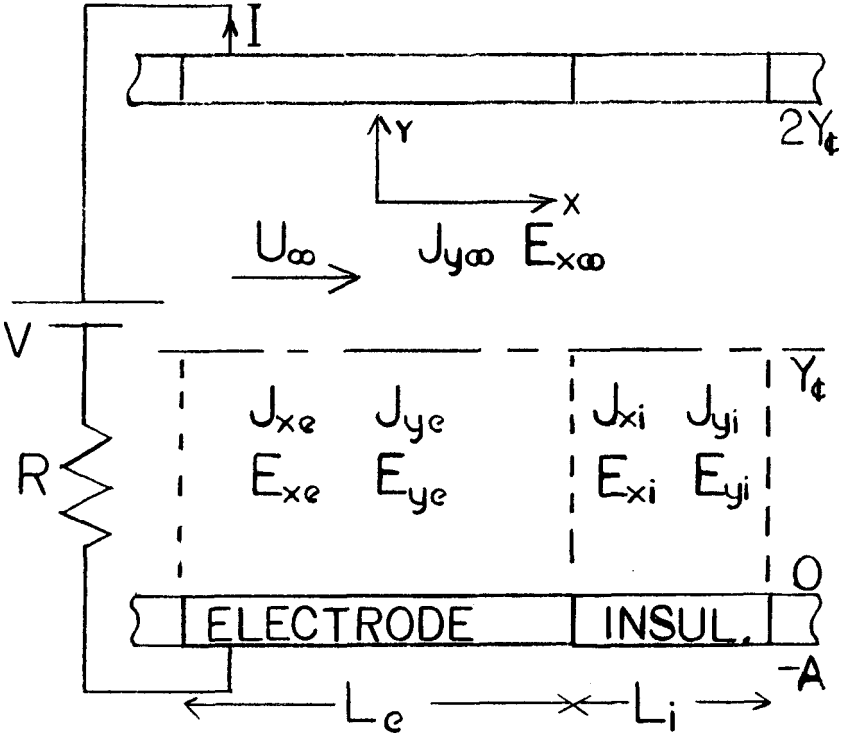

Figure 4-1. Generator configuration used in electrode current concentration plasma electrical model.

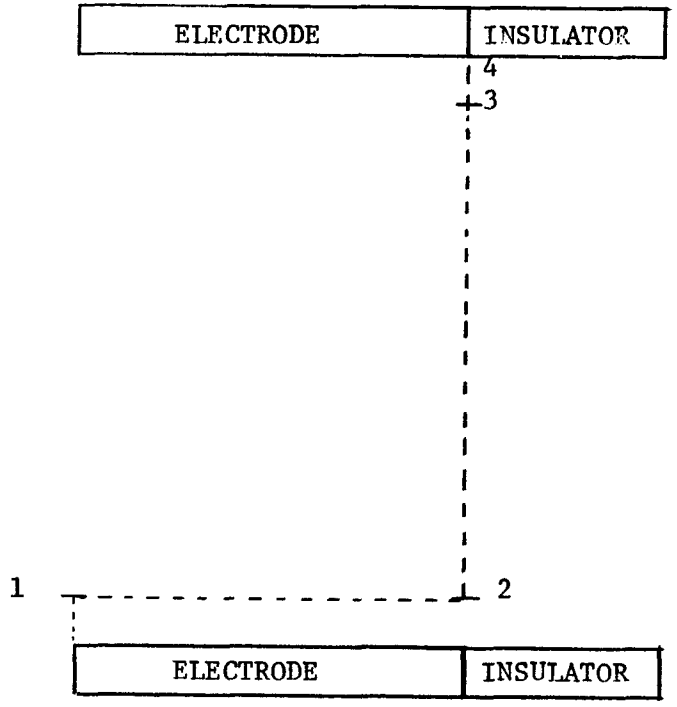

1: $V = V_o$

2: $V = V_o - E_{x\infty} Le$

3: $V = V_o - E_{x\infty} Le - 2\int_{\delta}^{Y_c} E_{y\infty}\, dy$

4: $V = 2V_o - E_{x\infty} Le - 2\int_{\delta}^{Y_c} E_{y\infty}\, dy$

Figure 4-2. Integration path for the electric field in the electrode current concentration plasma electrical model.

By employing Eqs. 4.1 through 4.10, we obtain the following results for V_o, $F_{ye}(x)$, $J_{y\infty}$, and $E_{x\infty}$, thereby uniquely defining the plasma currents and electric fields:

$$V_0 = - \left[\int_o^{Le} \frac{dx}{C_1(x)}\right]^{-1} \left[\int_o^{Le} \left[\frac{J_{y\infty}\, C_2(x)}{C_1(x)} + \frac{\left[C_4(x) - E_{x\infty}(x + C_3(x))\right]}{C_1(x)}\right]dx \tag{4.11}$$

$$F_{ye}(x) = \frac{-C_2(x)}{C_1(x)} - \frac{\left[V_0 - E_{x\infty}\, x + C_4(x) - E_{x\infty}\, C_3(x)\right]}{J_{y\infty}\, C_1(x)} \tag{4.12}$$

$$J_{y\infty} = - \left[\frac{C_8}{C_9}\left[Le - 2\, C_5(Le)\right] + 2\, C_6(Le) + (Le + Li)\, wR\right]^{-1} \left[V - 2\, V_0 + 2\, C_7(Le) - \frac{Li\, I_{xins}\left[Le - 2\, C_5(Le)\right]}{C_9}\right] \tag{4.13}$$

$$E_{x\infty} = \frac{J_{y\infty}\, C_8 - Li\, I_{xins}}{C_9} \tag{4.14}$$

The coefficients in Eqs. 4.11 through 4.14 are given below:

$$C_1(x) = \int_o^{\delta} \left(\frac{1 + \beta^2}{\sigma}\right)(1 - \phi(y))dy \tag{4.15}$$

$$C_2(x) = \int_o^{\delta} \left(\frac{1 + \beta^2}{\sigma}\right)\left(\phi(y) + \left(1 + {}^{Li}/_{Le}\right)(1 - \phi(y))\right)dy \tag{4.16}$$

$$C_3(x) = \int_o^{\delta} \beta\phi(y)dy \tag{4.17}$$

$$C_4(x) = \int_o^{\delta} uBdy \tag{4.18}$$

$$C_5(Le) = \int_{\delta}^{Yc} \beta\, dy\Big|_{x=Le} \tag{4.19}$$

$$C_6(Le) = \int_{\delta}^{Yc} \left(\frac{1 + \beta^2}{\sigma}\right)dy\Big|_{x=Le} \tag{4.20}$$

$$C_7(Le) = \int_{\delta}^{Yc} uB\, dy\Big|_{x=Le} \tag{4.21}$$

$$C_8 = \int_o^{Yc} \int_o^{Li} \beta\phi(y)dy\, dx \tag{4.22}$$

$$C_9 = \int_o^{Yc} \int_o^{Li} \sigma\left[\phi(y) + \left(1 + {}^{Le}/_{Li}\right)(1 - \phi(y))\right]dy\, dx \tag{4.23}$$

$$I_{xins} = \int_{-A}^{0} J_{xi}\, dy \tag{4.24}$$

In the above equations $\phi(y)$ is a matching function, also used by Oliver, which varies from zero at the wall to unity at the edge of the boundary layer. In this work, it is assumed that ϕ varies linearly between these two extremes. The boundary layer thickness is taken to be the minimum of the δ_{qq} boundary layer thickness, the electrode length and the insulator length.

4.1.2 Plasma Current Streamline Solution

In the plasma current streamline model, the exact two-dimensional equations governing current flow in the plasma are solved. For the lower portions of the boundary layer closest to the wall, an integro-differential equation is solved, in place of the more conventional partial differential equation. This provides stability and accuracy in the numerical implementation of the model. For the remainder of the plasma, the conventional two-dimensional partial differential equation is solved. In the following paragraphs the theoretical equations and boundary conditions employed in the model will be described.

The differential equation for current conservation is automatically satisfied by introducing the current stream function Ψ. The differential equation in vector form and its two-dimensional counterpart are given below.

$$\vec{\nabla} \cdot \vec{J} = 0 \tag{4.25}$$

$$\frac{\partial J_x}{\partial x} + \frac{\partial J_y}{\partial y} = 0 \tag{4.26}$$

Equation 4.25 is satisfied by assuming the following functional dependence of the plasma currents on the stream function.

$$J_x = {}^{\partial\Psi}/_{\partial y} \tag{4.27}$$

$$J_y = - {}^{\partial\Psi}/_{\partial x} \tag{4.28}$$

Introducting Eqs. 4.27 and 4.28 into Ohm's law for the plasma results in the following equations

$$E_x = \left(\frac{1}{\sigma}\right)\left(\frac{\partial \Psi}{\partial y} - \beta \frac{\partial \Psi}{\partial x}\right) \tag{4.29}$$

$$E_y = + uB - \left(\frac{1}{\sigma}\right)\left(\frac{\partial \Psi}{\partial x} + \beta \frac{\partial \Psi}{\partial y}\right) \tag{4.30}$$

For the plasma region outside the lower extremes of the boundary layer, the following differential equation is applied.

$$\vec{\nabla} \times \vec{E} = 0 \tag{4.31}$$

The two-dimensional counterpart to this equation is

$$\frac{\partial E_y}{\partial x} - \frac{\partial E_x}{\partial y} = 0 \tag{4.32}$$

Substitution of Eqs. 4.29 and 4.30 into 4.32 results in the following second order partial differential equation for the current stream function.

$$\begin{aligned} &\frac{\partial^2 \Psi}{\partial x^2} + \frac{\partial^2 \Psi}{\partial y^2} + \frac{\partial \Psi}{\partial x}\left(-\frac{1}{\sigma}\frac{\partial \sigma}{\partial x} + \frac{\beta}{\sigma}\frac{\partial \sigma}{\partial y} - \frac{\partial \beta}{\partial y}\right) \\ &\quad + \frac{\partial \Psi}{\partial y}\left(-\frac{\beta}{\sigma}\frac{\partial \sigma}{\partial x} - \frac{1}{\sigma}\frac{\partial \sigma}{\partial y} + \frac{\partial \beta}{\partial x}\right) - \sigma \frac{\partial}{\partial x}(uB) = 0 \end{aligned} \tag{4.33}$$

This equation is used for the region outside the lower extremes of the boundary layer.

Within the lower extremes of the boundary layer, the integral form of Eq. 4.31 is employed.

$$\int \vec{E} \cdot \vec{dL} = 0 \tag{4.34}$$

When applied to a local rectangular region, Eq. 4.34, with the use of Eqs. 4.29 and 4.30 becomes the following.

$$\begin{aligned} &\int_{y_1}^{y_2} \left\{\left[uB - \frac{1}{\sigma}\left(\frac{\partial \Psi}{\partial x} + \beta \frac{\partial \Psi}{\partial y}\right)\right]_{x_1} - \left[uB - \frac{1}{\sigma}\left(\frac{\partial \Psi}{\partial x} + \beta \frac{\partial \Psi}{\partial y}\right)\right]_{x_2}\right\} dy \\ &\quad + \int_{x_1}^{x_2} \left\{\left[\frac{1}{\sigma}\left(\frac{\partial \Psi}{\partial y} - \beta \frac{\partial \Psi}{\partial x}\right)\right]_{y_2} - \left[\frac{1}{\sigma}\left(\frac{\partial \Psi}{\partial y} - \beta \frac{\partial \Psi}{\partial x}\right)\right]_{y_1}\right\} dx = 0 \end{aligned} \tag{4.35}$$

Due to the elliptic nature of the governing equations for the current stream function, the boundary conditions must be specified on all the

boundaries. A sketch of the calculation region and its boundaries can be found in Fig. 4.3.

Along the electrode surface we require that the axial electric field vanish. Equation 4.29 thereby produces the following constraint on the stream function at the electrode surface.

$$\frac{\partial \Psi}{\partial y} - \beta \frac{\partial \Psi}{\partial x} = 0 \tag{4.36}$$

In addition we have the following two constraints on the stream function at the electrode edges.

$$\Psi(0,0) = 0.0 \tag{4.37}$$

$$\Psi(Le,0) = - \int_0^{Le} J_y(x,0)dx = - \overline{J}_{y\infty}(Le + Li) \tag{4.38}$$

$J_{y\infty}$ in Eq. 4.38 is a specified average core transverse current density. Equations 4.37 and 4.38 ensure transverse current conservation globally.

The insulator boundary condition is that the transverse current density vanish at the surface; this leads to the following constraint along the insulator surface.

$$\Psi(x,0) = - \overline{J}_{y\infty} (Le + Li) \tag{4.39}$$

for $Le < x < Le + Li$

At the plasma centerline, we enforce the condition that the current streamlines be antisymmetric. This results in the following equations for the electrode region.

$$\frac{\partial \Psi}{\partial y} (x,y_c) = \frac{\partial \Psi}{\partial y} (Le - x,y_c) \tag{4.40}$$

$$\Psi(x,y_c) + \Psi(Le - x,y_c) = - \overline{J}_{y\infty} (Le + Li) - 2 I_{xins} \tag{4.41}$$

for $0 < x < Le$

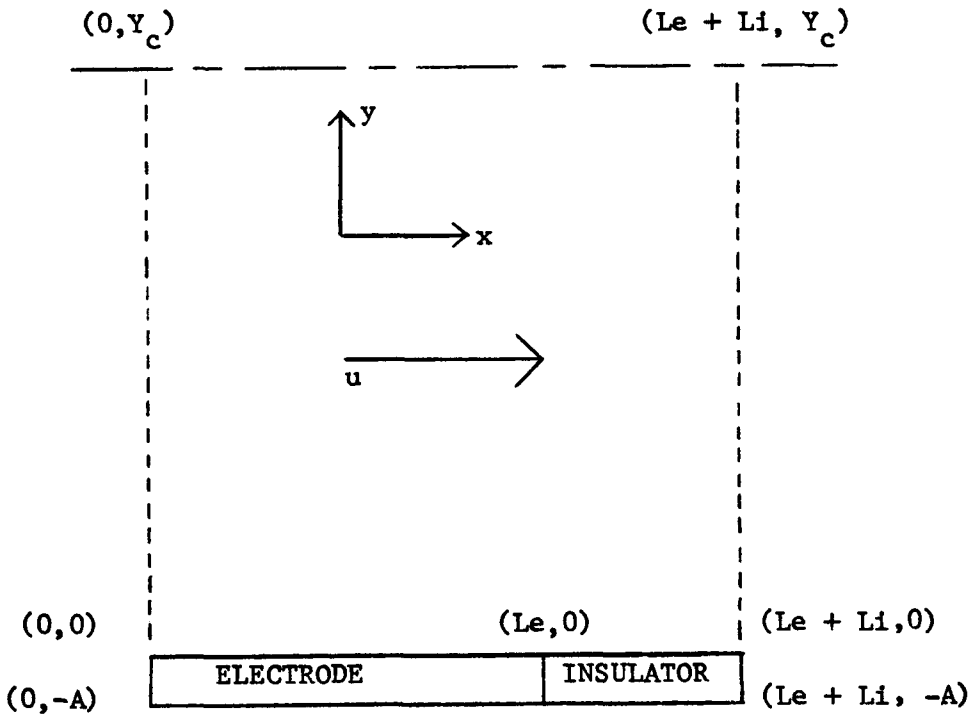

Figure 4-3. Generator configuration used in plasma current streamline solver.

For the insulator region we have the analogues relations listed below.

$$\frac{\partial \Psi}{\partial y}(x,y_c) = \frac{\partial \Psi}{\partial y}(2\ Le + Li - x, y_c) \tag{4.42}$$

$$\Psi(x,y_c) + \Psi(2\ Le + Li - x, y_c) = -2\ \bar{J}_{y\infty}(Le + Li) - 2\ I_{xins} \tag{4.43}$$

for $Le < x < Le + Li$.

In Eqs. 4.41 and 4.43, the insulator axial current leakage is explictly included to enforce the constraint that the net axial current must vanish at the axial position corresponding to the insulator midpoint.

At the transverse boundaries, we solve either Eq. 4.33 or Eq. 4.35 through the boundary, employing the following periodic constraint when necessary.

$$\Psi(x,y) = \Psi(x + Le + Li, y) + \bar{J}_{y\infty} (Le + Li) \qquad (4.44)$$

The numerical scheme employed in the solution of the above equations consists of successive over relaxation with a variable over relaxation factor. The magnitude of the over relaxation factor is calculated by the program based on the sign of the error at a fixed node in the plasma. Implicit axial line relaxation is utilized for speed and stability during the initial stages of the calculation.

A number of steps have been taken to maximize the stability, speed and accuracy of the numerical algorithm. These include using implicit methods and solving integro-differential equations where appropriate, such as Eq. 4-35.

4.2 Electron Energy Equation

To provide accuracy and numerical stability in the calculation of the electron temperature in a combustion driven MHD plasma, especially under high electrical loads, it is necessary to retain more terms in the electron energy equation than the usual Joule heating and collisional loss terms. In the present model, four terms have been retained: convection, transverse diffusion, Joule heating and collisional losses. The collisional loss term accounts for both elastic and inelastic collisions with the combustion products. The differential electron energy equation is presented below.

$$\left[u \frac{\partial}{\partial x} + v \frac{\partial}{\partial y}\right]\left[n_e\left(\frac{3}{2} kT_e + \varepsilon_i\right)\right] - \frac{\partial}{\partial y}\left(K_y \frac{\partial T_e}{\partial y}\right) - J^2/\sigma + 3n_e k \left(T_e - T_h\right) \delta_i \left(\frac{e}{m_h \mu_e}\right) = 0 \qquad (4.45)$$

δ_i, the inelastic collision loss factor is taken to be a constant, typically around 2000 for combustion gases. The transverse conduction coefficient, K_y, is obtained from simple kinetic theory considerations

$$5\left(\frac{k\mu_e}{e}\right)\left(n_e k\, T_e\right) \qquad (4\text{-}46)$$

The imposed transverse boundary conditions are that the electron temperature equal the bulk plasma temperature at both the centerline and at the wall. The initial condition is obtained by equating the electron temperature profile to the bulk plasma temperature profile in a region with no current.

The numerical algorithm is fully implicit in the transverse direction and marches in the axial direction. In order to obtain accuracy especially in regions of the plasma with large axial gradients, the electron energy and continuity equations in addition to the bulk plasma energy equation are solved iteratively at each axial position.

4.3 Electrode Configuration Study

The current thrust of the work is directed at investigating the feasibility of a rod-type electrode, transverse to the plasma flow, for use in an open-cycle MHD generator. Previous consideration of rod electrodes [4.4, 4.5] has been aimed mainly at their use in closed cycle, non-equilibrium generators. For open-cycle MHD, transverse rod electrodes offer the possibility of a more uniform distribution of electrode current, thus reducing both electrode surface erosion and the tendency toward Hall field breakdown.

Any electrode raised into the flow stream will change the hydrodynamics of MHD flow. The flow over an array of rods in the boundary layer is complicated and very difficult to characterize analytically. However, from an engineering standpoint the important fluid mechanical question is what additional pressure drop rod electrodes will introduce into the generator.

Flow experiments in an open water channel were performed in order to address this question. The tests were run 7.5 meters downstream in a channel with about 0.5 m water depth and approximately 0.5 m/s mean velocity. These conditions gave a Reynolds number based on length of approximately 3.5×10^6, which is comparable with full scale MHD Reynolds numbers. The electrodes were represented by 1.3 cm diameter cylindrical wooden dowels spaced axially at 2.5 cm intervals and mounted 1 cm off the floor of the channel. These dimensions would likely be typical for rod electrodes in a large MHD channel. The ratio of boundary layer thickness ($\delta_{.99}$) to rod diameter was approximately 10. This ratio is the important geometric parameter if the rods behave like large scale wall roughness elements, and is again reasonable for a large MHD channel.

Velocity profiles upstream and downstream of the rod array were taken using a pitot probe, and friction coefficients were calculated. The friction coefficient is defined by $\bar{\tau}_{wall,app.} / \frac{1}{2} \rho U_\infty^2$, where $\bar{\tau}_{wall,app.}$ is the apparent average wall shear stress, i.e. the equivalent wall shear stress for a flow without rods but for which the total drag (pressure drag and skin

friction) is the same. A plot of the measured friction coefficients is shown in Fig. 4-4. For an array of 55 rods (55 inches in length @ 1 inch pitch) the effective friction coefficient is $C_f = 0.054$.

To investigate what effect the rod shape has on the drag induced by the array of rods, elliptical rods with a major-minor axis ratio of approximately 8 to 5 were used as a test case for comparison. The rod dimension in the flow direction was kept the same as the diameter of the cylindrical rods, while the dimension perpendicular to the flow was reduced. As expected, this decreased the total drag, and the friction coefficients for the same number of cylindrical rods decreased by a factor of about 2.

No attempt has yet been made at parametrizing the effects of varying the rod dimensions, distance of the rods from the wall, or the spacing between rods. For a large array of rods (say 5 meters long in a large MHD channel) the curves indicate that an effective average friction coefficient of 0.01 should be easily achievable. In comparison, for an MHD flow in a 7 meter (flat electrode) channel with a roughness height of 3 mm, Ahluwalia and Doss [4.6] predict analytically an average friction coefficient of about $\overline{C}_f = 0.005$. Whether or not 3 mm is typical for channel roughness, it seems reasonable to expect that the drag due to rod-type electrodes can be reduced by further design improvements to an acceptable range, if it can be shown there is an advantage in using this type of electrode.

Electrical current distributions are being calculated using a two dimensional MHD electrical code. To move forward rapidly in designing an MHD experiment, the rod electrode is being modeled (as a first cut) as a polygon. A program using a full coordinate transformation, to account for the circular electrode shape within a rectangular domain, will be written in the near future. However, for our present needs, the existing program gives very adequate results.

Figure 4-5 shows, as a function of length, the cumulative fraction of total current collected by a 1.3 cm. diameter rod electrode within a Faraday channel of total height 10 cm. The first distribution is for a plasma of uniform electrical conductivity. The second distribution shows the effect of a 100 to 1 linear variation (in the vertical or y direction) in conductivity from approximately the top of the electrode to the wall. While the actual conductivity field around a rod electrode will be much more complicated than a

VARIATION OF FRICTION COEFFICIENT

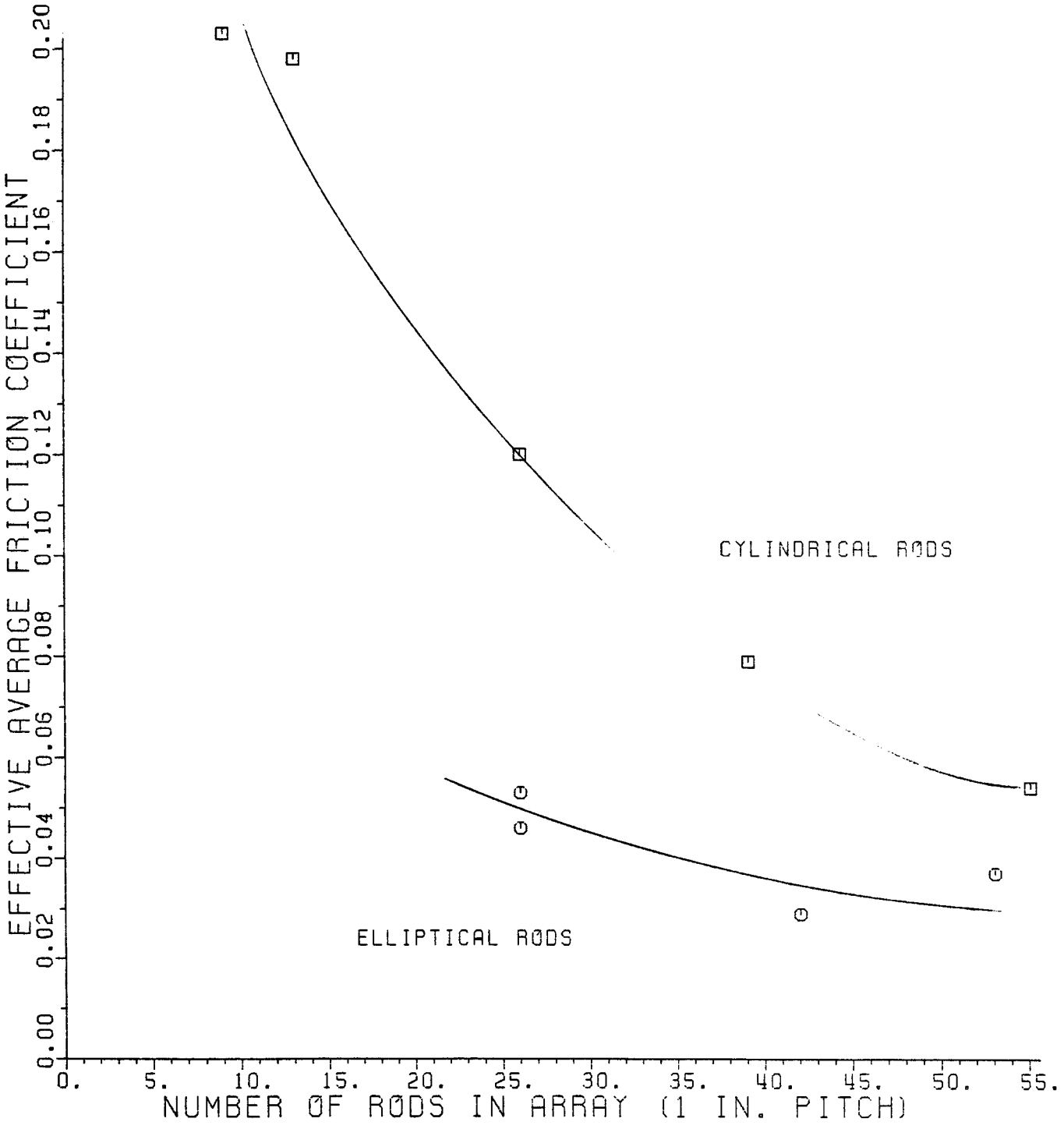

Figure 4-4. Effective friction coefficients for arrays of cylindrical and elliptical rods

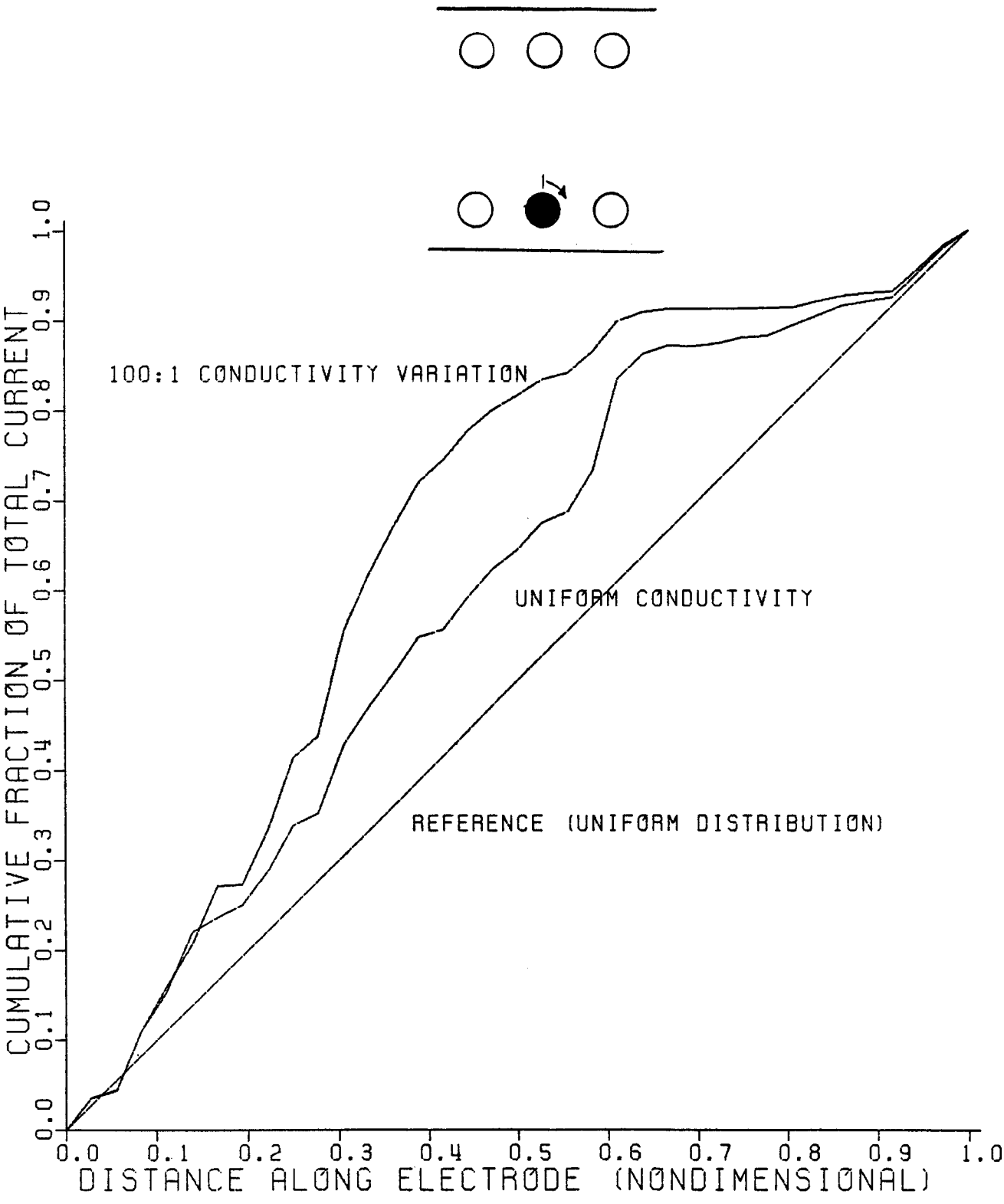

Figure 4-5. Cumulative fraction of total rod electrode current as a Function of distance along rod circumference.

simple y variation, Fig. 4-5 shows that the distribution of current is relatively insensitive to the conductivity field (much less sensitive than a flat electrode). A similar insensitivity was found for the effect of variations in the velocity field. These findings are important qualitative results, and should be useful in extending the validity of experimental current distributions.

Work in the immediate future will include designing and constructing a electrically segmented rod electrode, so that current distributions can be measured in the Stanford M2 channel. These measurements will be compared with results from more accurate computer modeling (using a coordinate transformation) of the current flow. Ultimately, the goal is to compare the results of Hall field breakdown experiments for rod electrodes with those of flat electrodes.

5.0 SIX TESLA MAGNET STUDIES

5.1 Disk Generator Studies

5.1.1 Six-Tesla Disk Generator Experiment

A series of thermal testing of the six-Tesla disk generator facility with the peg wall test section have been successfully completed. The purpose of the test is to operate the facility under the full thermal and electrical conditions prior to the experiment with the super-conducting magnet.

Two separate tests have been conducted for unseeded and seeded conditions. Thermodynamic and electrical parameters of the combustion gas and the test section conditions such as the peg surface temperature, the heat flux to the wall and the electrical insulation of the channel were obtained. The current discharge experiments were also conducted to provide reference data for the zero magnetic field condition. At the writing of this report data are being analyzed to define objectives of full scale experiments with the super-conduction magnet.

5.1.2 Boundary Layer Studies

Extensive numerical studies of the disk generator boundary layer phenomena have been conducted using two-dimensional finite difference computer codes. Some of the results are summerized in a Ph.D. thesis, "Performance of Combustion Disk MHD Generator". [5.1].

The integral method layer codes have been combined with quasi-one-dimensional performance calculation codes. Several of numerical calculations to evaluate full-scale disk generator have been conducted. The results are currently being analyzed in reference to results of the two-dimensional finite difference codes.

5.2 Linear Generator Studies

The electrical data of the linear channel experiment were analyzed with a one-dimensional model. This model was developed with the Investigative Data Analysis (IDA) techniques described in Ref. [5.2]. Good agreement was found between predicted and measured plasma electrical conductivities. The model also predicted low electrical resistance in the axial direction between electrodes. A two-dimensional electrical code is being modified to permit

comparison of two-dimensional calculations with one-dimensional calculations and experimental results.

A one-dimensional Rosa type model which included axial current leakage was developed for a segmented Faraday generator. The following assumptions were made:

1) Variations of quantities in the magnetic field and axial directions are ignored.
2) The Hall parameter (β) is constant.
3) The magnetic field (B) is constant.

For this model the equations are:

$$j_y = (\langle u \rangle_{yz} \; B - \frac{V_E}{h} + \beta E_x)/(1 + \beta^2)\langle \sigma - 1 \rangle_{zy}$$

$$\langle \sigma \rangle = (\beta d_y + \langle j_x \rangle_{yz})/E_x$$

Using measured currents and voltages (Faraday and Hall) and an assumed temperature profile shape the average conductivity, $\langle \sigma \rangle$, and the axial leakage resistance can be predicted. Good agreement was found in predicted and measured average plasma conductivity with a one-fifth power law temperature profile. The results are weakly dependent on boundary layer thickness. The use of a one-fifth temperature profile is consistent with the higher than expected voltage drops and channel shape.

As previously described in Ref. [5.3] deposits were discovered on the channel wall following the linear channel experiments. These deposits appear to have affected channel performance. The computer code NPSE, developed by Ron Nelson, Ref. [5.4] is being modified to allow two-dimensional channel calculations with a non-slagging conductive layer on the electrodes. These results can then be compared with those of the one-dimensional model and the linear channel experiments.

6.0 REFERENCES

2.1 "A High Magnetic Field MHD Generator Program", Quarterly Report FE-15611-5 for the period Jan. 1, 1981 - March 31, 1981, Stanford University, pp. 4-7.

2.2 "A High Magnetic Field MHD Generator Program", Annual Report FE-15611-3 for the period Oct. 1, 1979 - Sept. 30, 1980, Stanford University, pp. 5-18.

2.3 Rose, R. J., "The Hall and Ion Slip Effects in a Nonuniform Gas", Physics of Fluids, Vol. 5, No. 9, 1962, pp. 1081-1090.

2.4 Oliver, D. A. and Mitchner, M., "Nonuniform Electrical Conduction in MHD Channels", AIAA Journal, Vol. 5, No. 8, 1967, pp. 1424-1432.

2.5 Barton, J. P., "Fluctuations in Combustion-Driven MHD Generators", Ph.D. Thesis, Stanford University, August 1980.

2.6 T. D. Simons, R. H. Eustis, and M. Mitchner, "Effects of Magnetic Interaction on Acoustic Waves in a Combustion MHD Generator", 19th Symposium on Engineering Aspects of MHD, Tullahoma, TN, June 1981.

2.7 " A High Magnetic Field MHD Generator Program", Quarterly Rep. on Contract No. DE-AC01-80E15611, FE-15611-4, Stanford University, January 1981.

2.8 T. D. Simons, "Effects of Magnetic Interaction on Acoustic Waves in a Combustion MHD Generator", thesis proposal, HTGL, Stanford University, October 1980.

2.9 J. P. Barton, J. K. Koester, and M. Mitchner, "Probe-Tube Microphone for Pressure-Fluctuation Measurement in Harsh Environment", J. Acoust. Soc. Am. 62, No. 5, 1312, November 1977.

3.1 Rankin, R. P., Self, S. A., Eustis, R. H., "Study of the Insulating Wall Boundary Layer in a Faraday MHD Generator", AIAA Journal, Vol. 18, No. 9, September 1980.

3.2 James, R. K., "Joule Heating Effects in the Electrode Wall Boundary Layer of MHD Generators", High Temperature Gasdynamics Laboratory Report No. 115, Department of Mechanical Engineering, Stanford University, January 1980.

3.3 Branover, H., "Magnetohydrodynamic Flow in Ducts", John Wiley and Sons, 1978.

3.4 Hua, Hs. M., Lykoudis, P. S., "Turbulence Measurements in a Magneto-Fluid-Mechanic Channel", Nuclear Science and Engineering, Vol. 54, p. 445, 1974.

3.5 Rankin, R. R., "Insulating Wall Boundary Layer in a Farraday MHD Generator", High Temperature Gasdynamics Laboratory, Department of Mechanical Engineering, April 1978.

3.6 Olin, J. G., "Turbulence Suppression in Magnetohydrodynamic Flows, "High Temperature Gasdynamics Laboratory SU-IPR Report No. 85, Department of Mechanical Engineering, Stanford University, July 1966.

3.7 Mayo, W. T. Jr., Shay, M. T., Riter, S., "The Development of New Digital Data Processing Techniques for Turbulence Measurements with a Laser Velocimeter", USAF Arnold Engineering Development Center Report No. AEDC-TR-74-53, August 1974.

4.1 "A High Magnetic Field MHD Generator Program", FE-15611-5, Quarterly Report 1/1/81 - 3/31/81, Stanford University, Stanford, California, April 1981.

4.2 Oliver, D. A., "The Prediction of Inter-Electrode Breakdown in MHD Generators", 14th Symposium on Engineering Aspects of MHD.

4.3 M. Mitchner and C. Kruger, Partially Ionized Gases, Wiley and Sons, New York, 1973.

4.4 Houben, J. W. M. A., Blowm, J. H., and Rietjens, L. H. Th., "The Effects of Electrode Configuration on the Performance of a Faraday Type MHD Generator", 12th Symposium on Engineering Aspcts of Magnetohydrodynamics, paper I.3, Argonne National Laboratory (1972).

4.5 Zarderer, B. and Tate, E., "High Enthalpy Extraction Experiments in a Large Non-Equilibrium MHD Generator", 13th Symposium on Engineering Aspectcs of Magnetohydrodynamics, paper I.4, Stanford University (1973).

4.6 Ahluwalia, R. K. and Doss, E. D., "Convective Heat Transfer in MHD Channels and its Influence on Channel Performance", AIAA 18th Aerospace Sciences Meeting, Pasadena, CA (1980).

5.1 Jenkins, Marion K., "Performance of Combustion Disk MHD Generators," Ph.D. Thesis, Mechanical Engineering Department, Stanford University, September 1981.

5-2 W. Unkel, et al., "Investigative Data Analysis Technique for MHD Generators," AIAA Paper No. 81-0174, AIAA 19th Aerospace Sciences Meeting, 1981.

5-3 Quarterly report, Oct. 1 - Dec. 31, 1980.

5-4. Nelson, R. M., "Electrical Effects of Slag in a Diffuse Mode Magnetohydrodynamic Generator," Ph.D. Thesis, Mechanical Engineering Department, Stanford University, (June 1981)

*U.S. GOVERNMENT PRINTING OFFICE: 1981-740-145/2791